

Robust Control of Miniaturized Optical Image Stabilizers for Mobile Phone Cameras

by

Alireza Alizadegan

B.Sc., Sharif University of Technology, 2014

A THESIS SUBMITTED IN PARTIAL FULFILLMENT OF
THE REQUIREMENTS FOR THE DEGREE OF
MASTER OF APPLIED SCIENCE

in

The Faculty of Graduate and Postdoctoral Studies
(Mechanical Engineering)

THE UNIVERSITY OF BRITISH COLUMBIA

(Vancouver)

August 2016

© Alireza Alizadegan 2016

Abstract

Cameras in mobile phones are the most popular due to their availability and portability; however, image blur caused by involuntary hand-shakes of the photographer degrades their image quality as mobile phones become lighter, smaller, and high-resolution. The *optical image stabilizer (OIS)* is a hardware-based alternative to conventional software-based de-blurung algorithms that offer superior de-blur; however, they are set back for mobile phone applications by cost, size, and power limitations.

The magnetically-actuated lens-tilting OIS is a novel miniaturizable and low-power conceptual design which is suitable for low-cost micro manufacturing methods; however, significant product variabilities caused by these methods, along with the strict performance requirements to outperform software-based algorithms, and the limited controller implementation capabilities of mobile phone devices pose a challenging control problem that is solved by the modeling and controller design method proposed in this thesis.

To solve the problem, practical manufacturing tolerances are simulated through computer-aided design and analyzed by finite-element methods to obtain the structure of the dynamics of OIS and uncertainties in dynamics. A dynamic uncertainty model is developed based on the analysis results and the robust H_∞ control theory is applied to guarantee the closed-loop stability and optimize the closed-loop performance against uncertainties with constrained controller order.

The proposed method is demonstrated in two steps. First, it is applied to a set of large-scale OIS prototypes to demonstrate its feasibility in an experimental setting and its capability to deal with physical product variabilities. Then, it is applied to a set of small-scale OIS prototypes containing mass-produced parts to verify its applicability to real OISs. In both cases, the experimental results suggest that the robust H_∞ controller outperforms the conventional nominal controllers and the μ -synthesis controller. By dealing with control challenges of the magnetically-actuated lens-tilting OIS, the application of this conceptual design to mobile phone cameras is expanded. Substitution of the conventional post-processing algorithms in mobile phone cameras with OIS has significant impact on their image quality.

Preface

This thesis is original intellectual property of the author, Alireza Alizadegan, working under supervision of Dr. Ryozo Nagamune and co-supervision of Dr. Mu Chiao. This work has been conducted in Control Engineering Laboratory and Micro-Electro-Mechanical Systems Laboratory at the University of British Columbia. The results presented are going to be submitted for publication.

The simulation-based results in Chapter 3 was published in the following conference proceedings:

- A. Alizadegan, P. Zhao, R. Nagamune, and M. Chiao. “Modeling and robust control of miniaturized magnetically-actuated optical image stabilizers.” in Proceedings of the IEEE International Conference on Advanced Intelligent Mechatronics (AIM), pp. 734-739., July 12-15, 2016.

Chapter 4 includes experimental results. In this chapter, first the proposed method is applied to large-scale prototypes in Section 4.3 to demonstrate feasibility of the proposed method in an experimental setting and its capability to deal with physical product variabilities. In application to large-scale OIS, the μ -synthesis controller is successfully implemented with robustness for the first time. This result was presented in the following conference proceedings:

- P. Zhao, A. Alizadegan, R. Nagamune, and M. Chiao. “Robust control of large-scale prototypes for miniaturized optical image stabilizers with product variations.” in Proceedings of the IEEE International Conference on Society of Instrument and Control Engineers of Japan (SICE), pp. 734-739., July 28-30, 2015.

Next, the large-scale results are extended by introduction of robust H_∞ controller, extensive comparison with different controller design methods, and frequency-domain closed-loop validations.

Preface

- A. Alizadegan, P. Zhao, R. Nagamune, and M. Chiao. “Robust control of miniaturized optical image stabilizers against product variabilities.” IEEE Transactions on Mechatronics.

Finally, to make experimental results more realistic, they are extended to small-scale OIS prototypes in Section 4.4 to show applicability of the proposed method to miniaturized OISs with mass-produced parts.

- A. Alizadegan, P. Zhao, R. Nagamune, and M. Chiao. “Application of Robust Control Method to Miniaturized OISs for Mobile Phone Applications.”, to be submitted for journal publications

Table of Contents

Abstract	ii
Preface	iii
Table of Contents	v
List of Tables	viii
List of Figures	ix
List of Acronyms	xi
Acknowledgements	xii
1 Introduction	1
1.1 Motivations	1
1.2 OIS Control System Architecture	3
1.3 Literature Review	3
1.3.1 Sensor-shifting OIS	4
1.3.2 Lens-tilting OIS	6
1.4 Controller Design Theories	9
1.4.1 Nominal Controller Design Methods	9
1.4.2 Robust Controller Design Methods	9
1.5 Research Objectives and Methodologies	10
1.6 Organization of Thesis	13
2 Optical Image Stabilizer	15
2.1 Mechanical Design	15
2.2 Control System Configuration	16
2.3 Performance Objectives and Specifications	17

Table of Contents

3 Robust Controller Design Method for OISs	19
3.1 Finite Element Analysis of Dynamics and Product Variability	19
3.2 Dynamic Uncertainty Modeling of OISs	22
3.3 Robust Controller Design for OISs	25
3.3.1 State-feedback Controller Design	29
3.3.2 Output-feedback Controller Design	29
3.4 Simulation Results	30
3.4.1 Modeling, Validation, and Robust Controller Design	30
3.4.2 Closed-loop Stability Analysis of Model Samples	32
3.4.3 Time- and Frequency-domain Performance Analysis	34
4 Experimental Results	39
4.1 Experimental Setups	39
4.1.1 Open-loop Frequency-domain System Identification	39
4.1.2 Closed-loop Time-domain Controller Implementation	40
4.1.3 Closed-loop Frequency-domain System Identification	41
4.2 Experimental Methodologies	42
4.2.1 System Identification Tests	42
4.2.2 Closed-loop Stability Tests	42
4.2.3 Time-domain Performance Tests	43
4.2.4 Frequency-domain Performance Test	44
4.3 Application to Large-scale OIS prototypes	44
4.3.1 Large-scale OIS Prototypes	44
4.3.2 Robust Control of Large-scale OIS Prototypes	46
4.3.3 Assessments of Robustness for Closed-loop Stability and Performance	47
4.4 Application to Miniaturized OIS Prototypes	53
4.4.1 Miniaturized OIS Prototypes	53
4.4.2 Robust Control of Miniaturized OIS Prototypes	55
4.4.3 Assessments of Robustness for Closed-loop Stability and Performance	57
4.5 Practical Implications of the Experimental Result	63
5 Conclusions	65
5.1 Summary	65
5.2 Contributions	68
5.3 Future Work	68
5.3.1 Multiple Robust H_∞ Control	68
5.3.2 Fixed-order Robust H_∞ Control	69
5.3.3 Implementation on Physical Mobile Phone Cameras	69

Table of Contents

Bibliography	70
-------------------------------	----

Appendices

A Controller Design Methodologies and Parameter Values	78
A.1 Notch Filter Design	78
A.2 PID Controller Design	79
A.3 Lead-lag Controller Design	80
A.4 LQG Controller Design	81
A.5 H_∞ Controller Design	82
A.6 Robust Controller Design	83
B Hand-shake Disturbance Database	85
B.1 Time-domain Signals	85
B.2 Frequency-domain Spectra	86
C Model Parameter Values	88
C.1 Uncertainty Model Parameter Values	88
C.2 Actuator Model Parameter Values	89

List of Tables

3.1	Summary comparison of μ -synthesis with Robust H_∞ on miniaturized OIS simulation model samples	36
4.1	Assessment of closed-loop stability robustness in large-scale OISs	49
4.2	Summary comparison of μ -synthesis with Robust H_∞ on large-scale OISs	51
4.3	Assessment of closed-loop stability robustness in miniaturized OISs	58
4.4	Summary comparison of μ -synthesis with Robust H_∞ on miniaturized OISs	60
4.5	Percent improvements achieved by robust H_∞ controller compared to conventional controllers for different case studies . .	63
A.1	Notch-filter design parameter values	78
A.2	Controller design parameters of the PID controller	80
A.3	Controller design parameters of the lead-lag controller	81
A.4	Controller design parameters of the LQG controller	82
A.5	Controller design parameters of the H_∞ controller	83
A.6	Controller design parameters of the μ -synthesis controller . .	83
A.7	Controller design parameters of the robust H_∞ controller . .	84
A.8	Summary of performance trade-offs associated with controller design parameters	84
C.1	Model parameter values	88
C.2	Moving-magnet actuator parameter values	89

List of Figures

1.1	Performance gap between software-based and hardware-based image stabilization approaches [18]	2
1.2	Principle of operation of lens-tilting and sensor-shifting OISs	2
1.3	Mobile phone camera coordinate system	3
1.4	The general OIS control system architecture	4
1.5	Mechanical design of a sensor-shifting OIS in one axis of image stabilization	4
1.6	Summary of limitations of the advanced control methods for the sensor-shifting OIS	5
1.7	The principle of operation of the liquid-lens OIS [54]	6
1.8	Mechanical design of a lens-tilting OIS [46]	7
1.9	The target experimental implementation layout for the proposed method	11
1.10	Thesis organization	14
2.1	Mechanical design of the miniature OIS [69]	16
2.2	Control system configuration of magnetically-actuated lens-tilting OIS in one axis of image stabilization	17
3.1	Eigen frequency analysis results	20
3.2	Nominal dynamics of OIS	21
3.3	Effect of uncertainties on tilting dynamics	23
3.4	Illustration of uncertainty region and definitions of uncertainty models	25
3.5	Weighted control system block-diagram	26
3.6	Model validation	31
3.7	Multi-model dynamic uncertainty model for FEA model of miniaturized OIS	32
3.8	Analysis of robust closed-loop stability of conventional controllers on OIS model samples	33
3.9	Time-domain performance assessment of different controllers on model samples of miniaturized OISs	35

List of Figures

3.10	Comparison of hand-shake disturbance suppression of the robust H_∞ controller with the PID controller in time-domain	36
3.11	Frequency response of transfer function from reference to tracking error on nominal model	37
3.12	Frequency response of transfer function from reference to control input on nominal model	38
4.1	The experimental setup	40
4.2	Open-loop frequency-domain system identification setup	40
4.3	Closed-loop time-domain controller implementation setup	41
4.4	Closed-loop time-domain controller implementation setup	42
4.5	Large-scale OIS prototype	45
4.6	Product variabilities in large-scale lens platforms	46
4.7	Frequency responses of large-scale OISs	47
4.8	Multi-model dynamic uncertainty model of large-scale OIS	48
4.9	Time-domain performance assessment of different controllers on large-scale OISs	50
4.10	Frequency response of transfer function from reference to tracking error on nominal model	52
4.11	Frequency response of transfer function from reference to control input on nominal model	53
4.12	Miniaturized OIS prototype	54
4.13	Product variabilities in miniaturized OISs	55
4.14	Frequency responses of miniaturized OISs	56
4.15	Multi-model dynamic uncertainty model of miniaturized OIS	57
4.16	Time-domain performance assessment of different controllers on miniaturized OISs	59
4.17	Frequency response of transfer function from reference to tracking error on nominal model	61
4.18	Frequency response of transfer function from reference to control input on nominal model	62
A.1	Weighted control system configuration H_∞ controller design	82
B.1	Time-domain signals of hand-shake disturbance database	86
B.2	Frequency-domain spectra of hand-shake disturbance database	87
C.1	Tilt actuation	89
C.2	Force-air-gap relationship ($i = 1$ A)	90

List of Acronyms

Symbol	Description
BMI	Bilinear matrix inequality
CAD	Computer-aided design
DOF	Degree of freedom
DSA	Dynamic signal analyzer
DSP	Digital signal processor
FEA	Finite element analysis
FEMM	Finite element method magnetic
LTI	Linear time-invariant
LMI	Linear matrix inequality
LQG	Linear quadratic Gaussian
LDV	Laser Doppler vibrometer
ICICS	Institute for Computing, Information and Cognitive Systems
OIS	Optical image stabilizer
mAh	milli-ampere hour
NSERC	Natural Sciences and Engineering Research Council
PID	Proportional-integral-derivative
RMS	Root mean square

Acknowledgements

This work was supported by the Natural Sciences and Engineering Research Council of Canada (NSERC) and the Institute for Computing, Information and Cognitive Systems (ICICS) at the University of British Columbia. I would like to thank my supervisor Dr. Ryozo Nagamune and co-supervisor Dr. Mu Chiao who tried their best to create a productive and informative research opportunity. My gratitude also goes to the members of Control Engineering Laboratory and Micro-electro-mechanical Systems Laboratory at the University of British Columbia for their kind assistance.

Chapter 1

Introduction

1.1 Motivations

Mobile phone cameras are optically mature technologies that have been finely tuned and optimized over the past decade to improve image quality by increasing pixel density [12]; however, image quality of mobile phone cameras is still inferior to that of point-and-shoot cameras [69].

The main source of the quality gap between mobile phone cameras and point-and-shoot cameras is the image blur due to involuntary hand-shakes of the photographer. As allowed space for OIS is smaller for mobile phones compared to point-and-shoot cameras, increasing pixel density leads to very small pixel size [61], and therefore longer exposure time is necessary to capture a certain amount of light. As exposure time increases, image quality becomes more affected by the blur caused by hand-shakes of the photographer during exposure time. Moreover, as mobile phone devices get lighter and smaller, they become more susceptible to hand-shakes of the photographer. Image stabilization is referred to techniques, either software-based or hardware-based, employed to alleviate this blur.

So far, majority of mobile phones industries implement software-based image stabilization algorithms [47] because it is an inexpensive, compact, and low-power solution; however, image quality is degraded during the post-processing. Research shows that this performance limit can only be improved through a hardware-based approach [18]. Figure 1.1 shows the performance gap between the software-based and hardware-based approaches to image stabilization. Hardware-based approach to image stabilization and the corresponding device are respectively called *optical image stabilization* and *optical image stabilizer (OIS)*.

OIS compensates for hand-shake by restoring image to its original position on the image sensor. This can be achieved by either tilting the lens or shifting the image sensor as illustrated in Figure 1.2. In order to replace software-based image stabilizers with OIS in mobile phone devices, robust feedback control against variabilities in low-cost miniaturized OISs plays a pivotal role.

1.1. Motivations

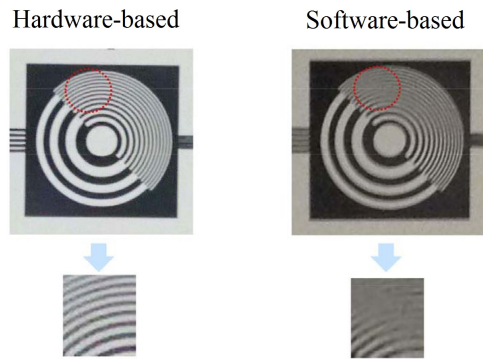


Figure 1.1: Performance gap between software-based and hardware-based image stabilization approaches [18]

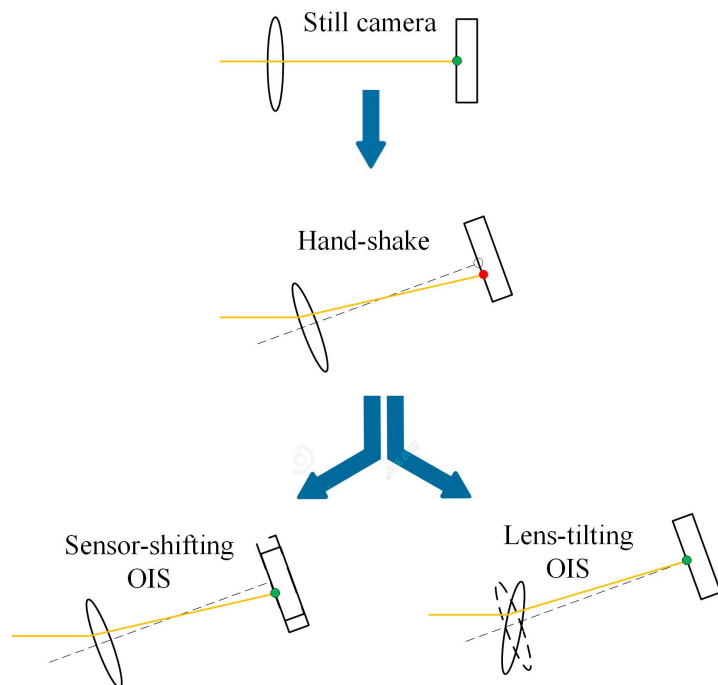


Figure 1.2: Principle of operation of lens-tilting and sensor-shifting OISs

1.2 OIS Control System Architecture

This section discusses the DOFs of OIS in a mobile phone device and their relationship with image blur. Then, a general control system architecture for OIS is introduced.

Involuntary hand-shakes of the photographer can occur all 6 DOFs of a mobile phone device. Figure 1.3 defines a coordinate system for a mobile phone camera. In this coordinate system only rotation about x - and y -axes are important for OIS. Rotation about z -axis and translation along none of the axes do not introduce image blur because they do not affect the position of the image on the image sensor.

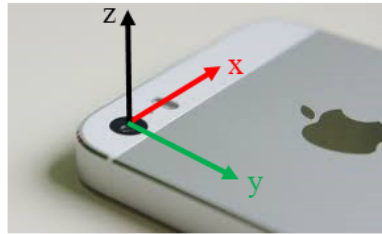


Figure 1.3: Mobile phone camera coordinate system

The block diagram of the general control system architecture is shown in Figure 1.4, where x - and y -axes in this figure refer to the coordinate system defined on the mobile phone device in Figure 1.3. As shown in Figure 1.4, similar independent feedback control loops are specified for each of x - and y -axes because typically OISs are symmetric with respect to x - and y -axis and the couplings between these two DOFs are negligible. In each loop, hand-shake is detected by gyro sensor of the mobile phone and passed through a signal processor that calculates the desired adjustment for the optical element. Then a standard feedback loop is used to drive the optical element to the desire position.

1.3 Literature Review

This chapter reviews existing works on OIS and its control. As introduced in Section 1.1, two main OISs applicable to mobile phone cameras are sensor-shifting OISs and lens-tilting OISs. In the following, we review mechanical design of each of these OISs, discuss their performance advantages and disadvantages, and point out their control challenges in the literature.

1.3. Literature Review

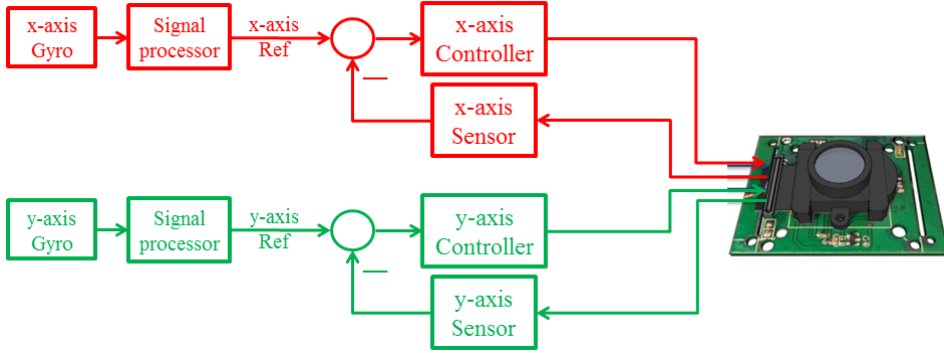


Figure 1.4: The general OIS control system architecture

1.3.1 Sensor-shifting OIS

So far, majority of OIS research has been focused on sensor-shifting design. The sensor-shifting OIS is size- and cost-efficient for large-scale cameras because it does not need to be replaced with the lens and actuate the heavy lens.

Figure 1.5 shows mechanical design of the sensor-shifting OIS. The image sensor is mounted on a moving frame. The moving frame can shift by ball bearings on a stationary frame, and is actuated by a voice coil motor (VCM).

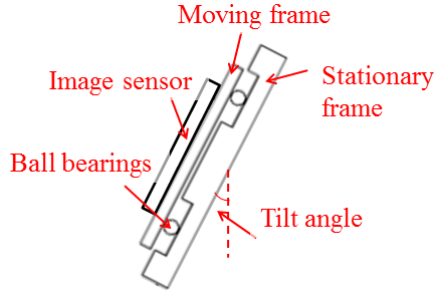


Figure 1.5: Mechanical design of a sensor-shifting OIS in one axis of image stabilization

The sensor-shifting OIS has miniaturization and performance limitations for mobile phone cameras. The VCMs used in sensor-shifting OIS are difficult to be miniaturized [29]. Besides, the hand-shake information gathered at the camera body might be different from that at the camera lens, and thus, performance of the sensor-shifting OIS is often inferior to that of lens-

1.3. Literature Review

tilting OIS [8].

In addition, the sensor-shifting OIS suffers from a challenging control problem due to friction disturbances caused by ball bearings and time-varying nonlinear dynamics due to VCM hysteresis and variations in the tilt angle as shown in Figure 1.5. Primarily, open-loop controllers have been used for position control of moving frame [32]; however, open-loop controllers cannot deal with friction disturbances inherent in ball bearings. Therefore, feedback controllers such as PID and lead/lag are preferred [64]. Moreover, voice coil motors (VCMs) has nonlinear dynamics which may dictate conservative controller design. To address this issue, a modified PID controller with a feedforward component was proposed to quickly respond to disturbances [31]. Another potential issue of sensor-shifting design is time-varying dynamics caused by time-varying effects of ball bearings and gravity on the moving frames. To cope with these dynamics variations, numerous techniques such as fuzzy [9], gain-scheduling [63], and sliding mode [45, 60, 66], adaptive [65] and a combination of these techniques [33, 34] have been employed to increase robustness of the closed-loop system against these variations; however, there are disadvantages corresponding to each of these methods as summarized in Table 1.6. Moreover, they yield a nonlinear/time-varying controller that might not be suitable for practical implementation on a mobile phone device with limited processing capabilities.

Author (Year)	Controller	Advantages	Disadvantages
Yeom et al. (2009)	Gain-scheduling	<ul style="list-style-type: none"> • Considers dynamics variations to improve performance 	<ul style="list-style-type: none"> • Needs measuring scheduling parameter • Identification of dynamics variations • Time-varying controller implementation
Yu et al. (2008)	Adaptive	<ul style="list-style-type: none"> • Adapts to time-varying dynamics • No <i>a priori</i> information of variations necessary 	<ul style="list-style-type: none"> • Adaptation may not converge quickly • Time-varying controller implementation
Li et al. (2012)	Sliding-mode	<ul style="list-style-type: none"> • Robust to nonlinearities • Guaranteed convergence time 	<ul style="list-style-type: none"> • Chattering needs careful actuator design • Non-trivial selection of sliding surfaces • Non-linear controller implementation

Figure 1.6: Summary of limitations of the advanced control methods for the sensor-shifting OIS

1.3. Literature Review

1.3.2 Lens-tilting OIS

For mobile phone cameras, a lens-tilting OIS may be a better option because the lens is lighter than the sensor, and thus easier to actuate, thereby expanding the battery life. In addition, since the lens is closer to the object than sensor, it requires smaller shifting for the same hand-shake. Finally, since the lens in mobile phone cameras will not be replaced, a lens-tilting OIS is not so cost-inefficient as it would be for professional cameras.

Based on this motivation, recently some conceptual designs have been proposed that relies on manipulation of the lens to achieve optical image stabilization. For instance, [54] proposed an OIS based on a liquid lens. The geometry of the liquid lens is adjusted by the electrowetting principles to control lens focal length and position to achieve optical image stabilization. The principle of operation of the liquid-lens OIS is illustrated in the Figure 1.7. In Figure 1.7, A shows the schematic of the liquid-lens principle where (o) is a drop of oil with α contact angle on an insulation coating of thickness d designated by the green line. The oil drop is surrounded by a conducting fluid (w). B and C are the images of the same oil drop on a parylene coating at 0 and 60V rms with 1 kHz frequency. The oil drop reacts to this excitation by changing the contact angle which in turn leads to change of the focal length and position for optical image stabilization.

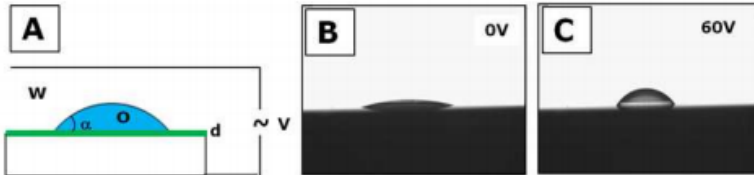


Figure 1.7: The principle of operation of the liquid-lens OIS [54]

The construction and miniaturization of the liquid lens assembly is quite elegant. It also has minimal hysteresis with properly designed liquid and coating; however, high speed (about 1 kHz) AC voltage fields (about 50 V) are required to drive the lens, which may need challenging circuit design. Furthermore, since liquid lens is involved, it might be quite difficult for the manufacturing process to obtain consistent results.

Recently, conceptual design of a novel lens-tilting OIS for mobile phone cameras focusing on size and cost has recently been published [46]. Figure 1.8 shows mechanical design of this lens-tilting OIS. The lens is held by a monolithic flat structure referred to as the lens-platform. The lens-

1.3. Literature Review

platform encompasses a plate supported by four folded beams connected to the base. The plate has the majority of the inertia of the system and folded beams work as linear springs providing sufficient stiffness for tilting of the plate. Damping comes merely from air damping and material damping that is fairly insignificant. The plate has 3 DOFs: two rotational DOFs about x -axis and y -axis for image stabilization as well as a translational DOF along z -axis for auto-focus. Actuation of 3 DOFs is achieved by four moving-magnet actuators installed at four corners of the device marked by 1–4 located in equal distances from central axes. Each moving-magnet actuator consists of a pair of coil and magnet. Magnets are attached to the lens platform whereas coils are fixed to the base. Actuation is achieved by forces generated on each magnet in response to the magnetic fields created by the current in its corresponding coil.

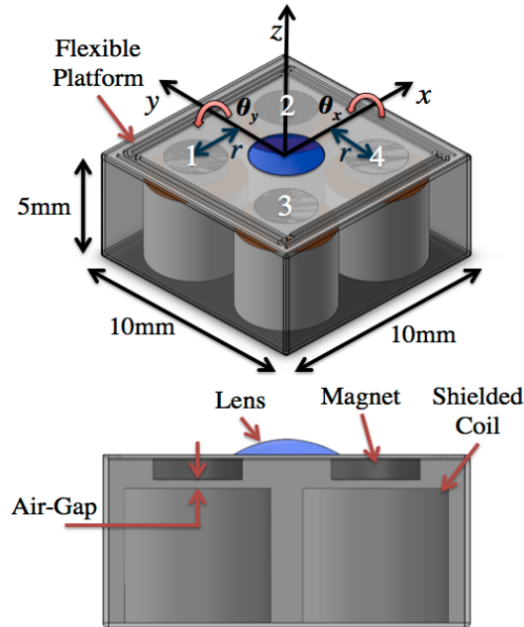


Figure 1.8: Mechanical design of a lens-tilting OIS [46]

This mechanical design has several advantages. Since the lens-platform is designed as a monolithic flat structure, it is suitable for cheap fabrication techniques such as micro-molding [21] and 3D printed molding [67]. In addition, it generates tilt actuation torque by a set of moving-magnet actuators. The moving-magnet actuators are smaller than common voice-coil-motor actuators [11, 29, 57] providing the same performance because of

1.3. Literature Review

the lighter moving part (magnets) and removal of moving wires compared to voice coil motors with moving coils. It is also faster, cheaper, and more power efficient than many other actuator types published in the literature such as thermal [10, 38], piezo-electric [28, 44] and moving-mirror [19], and shape memory alloy actuators. The miniaturizability and low-power characteristics of this conceptual design has been demonstrated on a MEMS scanner [55, 56]. The actuator force is nonlinear with respect to the distance between permanent magnet and the coil. However, this nonlinearity is substantially less compared to electrostatic and variable-reluctance actuators due to absence of ferromagnetic core in the center of the coil [4, 41, 50]. Friction mainly includes air-damping and material-damping causing minimal energy loss. Moreover, since OIS is mounted on the lens, hand-shake information on the lens are collected directly and used for compensation that promises better performance. Finally, no additional actuators are necessary for auto-focus as this design can simultaneously accomplish image stabilization and auto-focus by tilt and shift degrees-of-freedom (DOFs), respectively.

Despite the aforementioned advantages, there are two shortcomings concerning control of this device which has not been addressed in [46]: (1) A controller was designed for a 1 DOF prototype rather than the original 3 DOF conceptual design. (2) A controller was designed and tested on only one prototype rather than multiple prototypes. The 1 DOF prototype used in this work cannot capture full complexity and coupling of dynamics between different DOFs of the original 3 DOF conceptual design. Besides, the controller design approach used in this work completely ignores product variabilities which are inherent in cheap fabrication techniques for small-scale devices. Similar product variabilities are observed and considered in controller design for numerous similar small-scale devices in the past decade, such as single-stage [20] or dual-stage [13, 14, 22–25, 37, 42] hard disk drives micro-actuators, parallel-plate electrostatic micro-actuators [35, 71], micro/nano-positioning systems [30], micro-probes [59, 68], optical switches [26], gyroscopes [15, 16, 36], resonators [51, 52], relays [39], and capacitors [53]. These two shortcomings are specifically crucial for the magnetically-actuated lens-tilting design due to its inherent lightly-damped mechanical design. In lightly-damped systems, robust stability typically limits the bandwidth [1]. In addition, robust performance is essential for OIS application because improving the image blur in one product may deteriorate it in other platform. Covering these two shortcomings is the main topic of this thesis.

1.4 Controller Design Theories

The controller design theories used in this thesis are briefly reviewed in this section. For comparison purposes, the nominal controller design methods such as proportional-integral-derivative (PID), lead-lag, linear-quadratic Gaussian (LQG), and H_∞ controllers are introduced in Section 1.4.1. The robust control methods, being the emphasis of this thesis, is reviewed in Section 1.4.2.

1.4.1 Nominal Controller Design Methods

Nominal controllers in this thesis refer to controllers that only consider one plant (referred to as the nominal plant) in design stage. In industry, classical controller design methods such as PID and lead-lag controllers are typically employed mainly because they do not need model to for design, are simple to implement, and often generate satisfactory performance. However, these methods are inefficient in some applications because they are not necessarily an optimal controller design method. In addition, when designed without model, it is difficult to ensure closed-loop stability in the design stage. Therefore, they are typically used in series with notch filters to suppress the resonance modes of the plant.

To cover these two limitations, model-based controller design methods such as LQG and H_∞ control are introduced. LQG and H_∞ controllers are more complex compared to classical controllers, however they are designed optimally (in time-domain and frequency-domain, respectively). These methods also guarantee stability of the closed-loop system based on Lyapunov's quadratic stability theory through different mathematical formulations.

Despite a number of successful industrial applications, all these nominal controller design methods only take one plant into consideration in the design stage. More specifically, the closed-loop stability is not guaranteed and performance is not optimized against product variabilities.

1.4.2 Robust Controller Design Methods

Robust control theories explicitly deal with uncertainties in plants and disturbances through creating an uncertainty model [5, 6]. They typically formulate the robust controller design problem as an optimization problem where the constraint function represents closed-loop stability for the entire uncertainty set and the objective function represents the worst-case

1.5. Research Objectives and Methodologies

closed-loop performance considering uncertainties. Therefore, closed-loop stability can be guaranteed against product variabilities while optimizing the worst-case performance. These methods typically lead to a dynamic output-feedback linear time-invariant (LTI) controller that is easily implementable on mobile phones compared to adaptive or nonlinear controllers.

μ -synthesis is a conventional robust controller design method that handles parametric uncertainties for which there are numerically-efficient off-the-shelf algorithms available [3]; however, this method suffers from some limitations. Controller order and computational cost of design are typically high and increases drastically as the complexity of the robust control problem increases. This is typically dealt with model order reduction; however, model order reduction methods may not preserve robustness; therefore, tedious trial-and-error including order reduction and analysis should be performed to design a practically implementable controller. Since the order constraint was not imposed in the designed stage, the reduced-order controller is often far from optimal. Therefore, a small number of uncertainty parameters are desirable to model the uncertainties of the system which can lead to conservatism of the model. The controller designed based on a conservative model will have low closed-loop performance. In addition, the optimization problem associated with this method is non-convex. Non-convex optimization problems often yield conservative solutions. The conservativeness of the solution depends on the choice of initial guess; however, μ -synthesis does not provide any systematic means of solving for a decent initial guess. Furthermore, as uncertainties become larger and more complex, conservativeness, complexity, and computational cost of μ -synthesis increase.

1.5 Research Objectives and Methodologies

To take advantage of the lens-tilting OIS over software-based image stabilization in mobile phone devices, its control challenges (discussed in Section 1.3.2) summarized below should be addressed simultaneously:

- C1 strict tracking performance requirements to compete with software-based image stabilization methods in image de-blur;
- C2 low control effort requirements to compete with software-based image stabilization methods in battery life;
- C3 dynamics uncertainties due to product variabilities in low-cost micro-manufacturing of miniaturized devices;

1.5. Research Objectives and Methodologies

C4 low controller order requirements for practical implementation on mobile phone devices.

To overcome these challenges, the objective of this thesis is to develop a robust controller design method for the 3 DOF miniaturized conceptual design that is implementable in an experimental setting as illustrated in Figure 1.9.

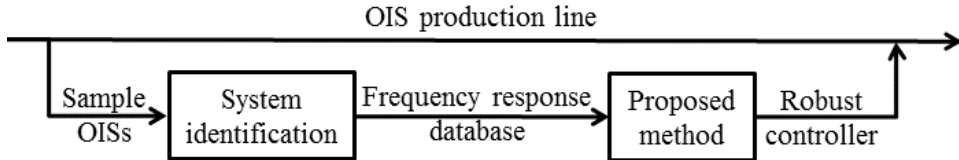


Figure 1.9: The target experimental implementation layout for the proposed method

Sample OISs are collected from the OIS production line and identified in frequency-domain to generate a frequency response database that represents dynamics uncertainties (C3). The frequency response database should be used by proposed method to design a robust controller that can be implemented in the original OIS production line. To safely implement the designed controller on the original production line, the proposed method should guarantee closed-loop stability for entire uncertainty region. To minimize conservatism of designed controller, the proposed method should optimize closed-loop performance against uncertainties (C1 & 2). Finally, the proposed method should constrain controller order for practical implementation on mobile phone device (C4).

To develop the controller design method and demonstrate performance of the designed controller, the following procedure is used:

1. Dynamics variations of 3 DOF miniaturized OISs are analysed under practical manufacturing tolerances by finite-element methods.
2. A robust controller design method is developed based on finite-element analysis results, mechanical design, and control objectives of OIS.
3. The proposed method is validated by creating uniform, comprehensive, and practical product variabilities using simulations.
4. An experimental methodology is developed to compare the performance of the robust controller with nominal controllers introduced in Section 1.4.

1.5. Research Objectives and Methodologies

5. Feasibility of the method in an experimental setting is tested by application to large-scale OISs with physical product variabilities using the experimental methodology.
6. Applicability of the method in real OIS production lines is proved by implementation on miniaturized OISs containing mass-produced parts.

1.6 Organization of Thesis

This section presents organization of the thesis as well as the interconnections between sections as illustrated in Figure 1.10.

In Chapter 2, details of lens-tilting OIS including its mechanical design (Section 2.1) is reviewed. Then, the control system configuration (Section 2.2) is described, and the control objectives and specifications (Section 2.3) are defined based on the research objectives defined in Section 1.5.

Chapter 3 presents the proposed method. In this chapter, Section 3.1 performs a finite element analysis (FEA) of dynamics and product variabilities on the OIS described in Section 2.1 based on its control system configuration proposed in Section 2.2. Then, Section 3.2 develops a dynamic uncertainty model based on the combination of finite element analysis results and mechanical design. Finally, robust controller design method is proposed in Section 3.3 to deal with the dynamic uncertainty model. There, the robust control theories introduced in Section 1.4.2 are applied considering control objectives and control system configuration to design the controller.

Chapter 4 presented the experimental results and discussions. In this chapter, Section 4.1 describes the experimental setups used for system identification (Section 4.1.1) and closed-loop implementation in time-domain (Section 4.1.2) and frequency-domain (Section 4.1.3). Then, some experimental methodologies are explained based on the setups for performing the tests and analysing the results, including system identification (Section 4.2.1), closed-loop stability (Section 4.2.2), and closed-loop implementation in time-domain (Section 4.2.3) and frequency-domain (Section 4.2.4). Then, the setups and methodologies are used to implement the method on large-scale (Section 4.3) and miniaturized (Section 4.4) OISs.

In Chapter 5, conclusions from experimental results are drawn (Section 5.1), contributions are summarized (Section 5.2), and outstanding research directions and potential future work are pointed out (Section 5.3).

Details of parameter values and supporting information are deferred to appendices. Appendix A reports design methodologies and resulting parameter values for baseline controllers. In Appendix B time-domain and frequency-domain data of hand-shake signals collected from a mobile phone device are presented. These data are first used in Section 2.3 to define control objectives and later in experimental setup to assess the performance of the proposed method.

Finally, Appendix C reports parameter values of the dynamic uncertainty models of the lens-platform as well as the moving-magnet actuators that are used in the proposed method.

1.6. Organization of Thesis

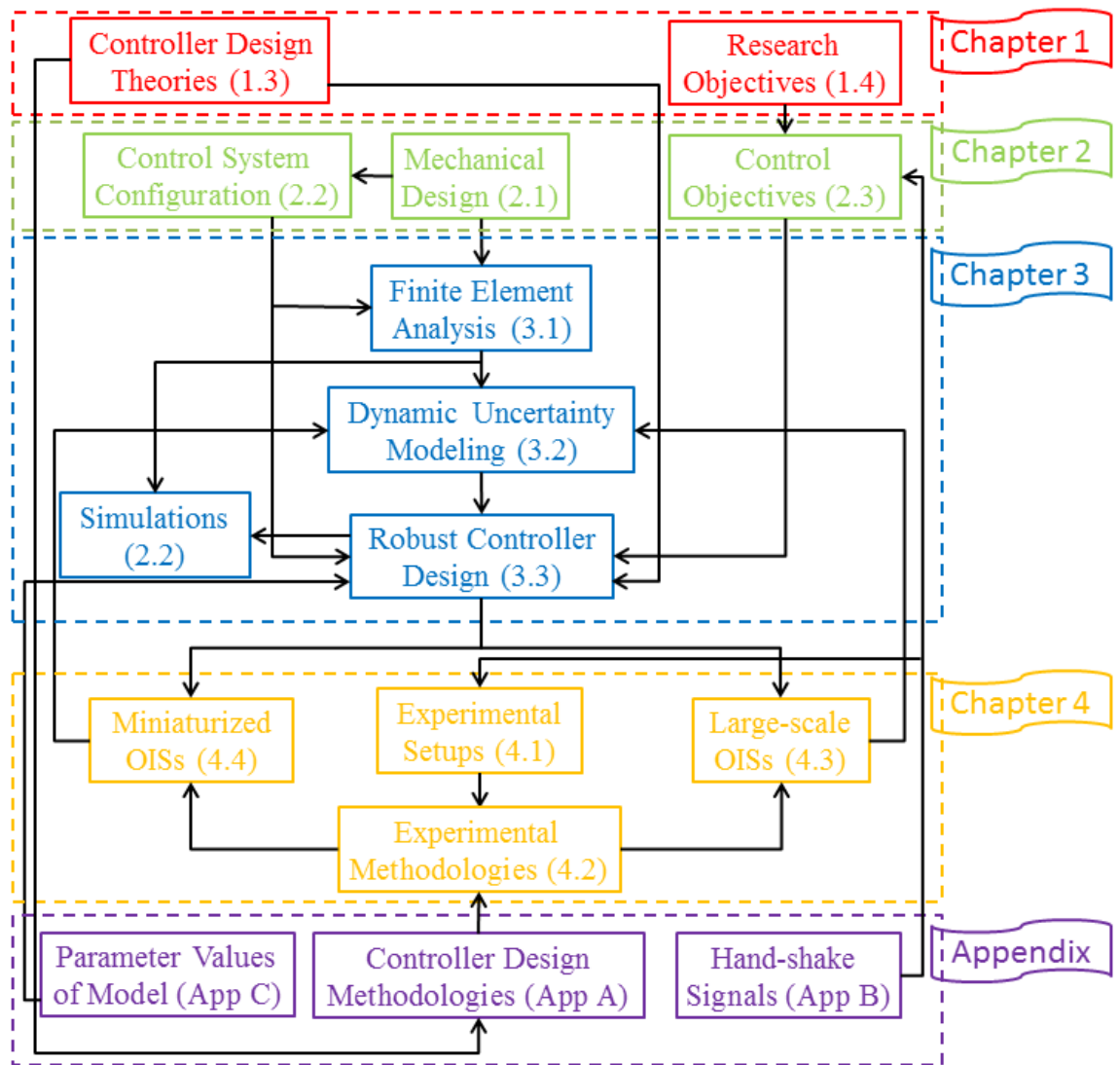


Figure 1.10: Thesis organization

Chapter 2

Optical Image Stabilizer

In this chapter, details of lens-tilting OIS including its mechanical design (Section 2.1), control system configuration (Section 2.2), and control objectives and specifications (Section 2.3) are reviewed.

2.1 Mechanical Design

Figure 2.1 shows a schematic for mechanical design of the miniature OIS presented in [46]. The lens is mounted a monolithic flat structure referred to as the lens-platform. The lens-platform encompasses a plate supported by four folded beams connecting the plate to the base. The plate has the majority of the inertia of the system and folded beams work as linear springs providing sufficient stiffness for tilting of the plate. Damping comes merely from air damping and material damping that is fairly insignificant. The plate has 3 DOFs: two rotational DOFs about x -axis and y -axis for image stabilization as well as a translational DOF along z -axis for auto-focus. Actuation of 3 DOFs is achieved by four moving-magnet actuators installed in four corners of the device marked by 1–4 located in equal distances from central axes. Each moving-magnet actuator consists of a pair of coil and magnet. Magnets are attached to the lens platform whereas coils are fixed to the base. Actuation is achieved by forces generated on each magnet in response to the magnetic fields created by the current in its corresponding coil. The coils' currents are the inputs and the motions corresponding to the 3 DOFs are the outputs of the OIS.

This conceptual design has pros and cons. The monolithic flat structure of the lens-platform makes it suitable for low-cost MEMS fabrication methods; however, these methods are afflicted by significant product variabilities. Besides, using moving-magnet actuators to achieve tilt actuation is a quite low-cost solution; however, couplings in dynamics of different DOFs can arise due to unavoidable asymmetry in fabrication of four independent moving-magnet actuators. Moreover, these couplings are uncertain because asymmetry of installation can appear in different ways for different products.

2.2. Control System Configuration

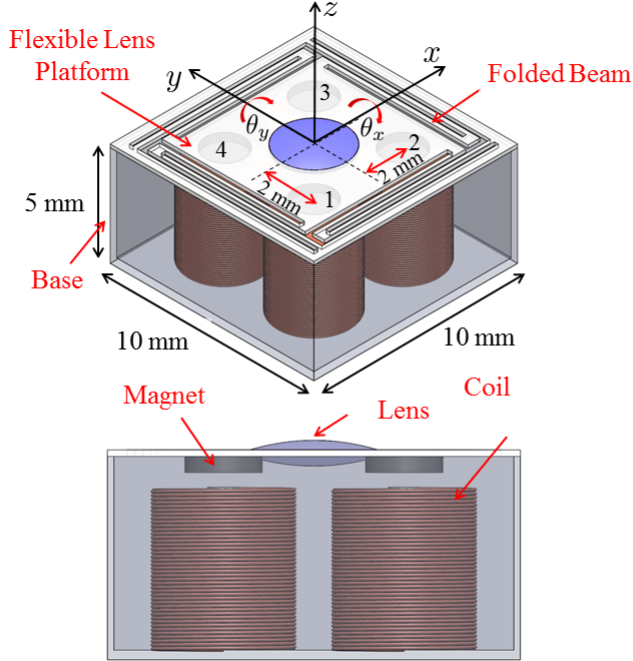


Figure 2.1: Mechanical design of the miniature OIS [69]

2.2 Control System Configuration

According to Section 1.2, as far as image stabilization is concerned, the control goal is to tilt the lens-platform about x -/ y -axis to a desired angle in an independent manner. Therefore, only one axis is considered hereafter. For each axis, the control goal is to use current of individual coils appropriately to tilt the lens-platform to a desired angle according to hand-shake disturbance data supplied by the mobile phone built-in gyro sensor. To achieve this goal, a control system configuration shown in Figure 2.2 was proposed in [46] specific for this OIS.

The hand-shakes disturbances are detected by the gyro sensor of the mobile phone and integrated once to obtain the tilt angle of the camera due to hand-shake. The camera angle is used to calculate, in ‘Signal processor’ block in Figure 2.2, the desired tilt angle of the lens that compensates for the tilt angle of the camera. The error signal is acquired by subtracting actual tilt angle from reference tilt angle. Based on the error, the controller sends appropriate current commands to four coils in order to tilt the lens-

2.3. Performance Objectives and Specifications

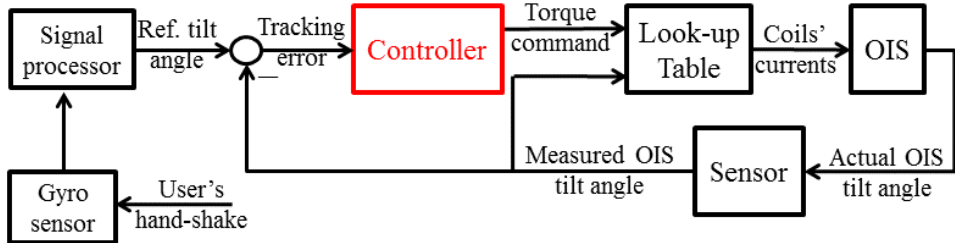


Figure 2.2: Control system configuration of magnetically-actuated lens-tilting OIS in one axis of image stabilization

platform for minimizing the error. The moving-magnet actuators described in Section 2.1 are non-linear; however, since non-linearity is static, the non-linearity is compensated for via a static map, that is the inverse of the map from the current to the torque. This is designated as ‘Look-up Table’ in Figure 2.2, and explained in detail in Appendix C. Therefore, throughout this thesis, controllers are designed by considering the torque as the control input, i.e the red box in Figure 2.2.

2.3 Performance Objectives and Specifications

The performance considerations proposed in this thesis include three specifications and three objectives. Performance specifications refer to hard constraints that have to be met, while performance objectives are performance measures that we wish to improve. Specifications are precedent to objectives and both are listed below in a descending order of priority. Performance specifications include:

- (S1) maximum of 1% steady-state error to ensure acceptable reference tracking and fair comparison of different controllers in this thesis,
- (S2) maximum of 6 dB peak sensitivity gain for closed-loop systems to allow sufficient stability margin for modeling errors,
- (S3) maximum of unity high-frequency controller gain to avoid control input saturation due to sensor noise amplification.

After satisfaction of performance specifications, the objectives are to:

- (O1) minimize tracking error to improve image blur,

2.3. Performance Objectives and Specifications

- (O2) minimize control effort to increase battery life,
- (O3) reduce controller order for practical implementation and computation power consumption considerations on a mobile phone.

These objectives and specifications are defined for a generic magnetically-actuated lens-tilting OIS; however, objective of the robust controller design method developed in the next section is to consider them for multiple OISs.

Chapter 3

Robust Controller Design Method for OISs

This chapter presents the proposed robust controller design method. In this chapter, first a finite element analysis of dynamics and product variabilities is performed on a computer-aided design (CAD) model of the OIS described in Section 2.1 based on its control system configuration proposed in Section 2.2 (Section 3.1). Then, a general dynamic uncertainty model is developed based on the combination of finite element analysis results and mechanical design (Section 3.2). Finally, robust control theories introduced in Section 1.4.2 are applied considering control system configuration as well as control objectives and specifications to deal with the dynamic uncertainty model.

3.1 Finite Element Analysis of Dynamics and Product Variability

To propose a physics-based dynamic uncertainty model in the next section, an FEA is performed in this section to identify dynamics of OIS as well as effect of uncertainties in beam width and actuator installation on dynamics of OIS. Figure 3.1 shows eigen frequency analysis results. There are four modes which are associated with four eigen frequencies denoted by ω_{n_i} , $i = 1, 2, 3, 4$. The first and second modes are respectively corresponding to shifting and tilting DOFs. The DOFs associated with the third and fourth mode are not trivial to explain based on mode shapes. Therefore, they are identified through performing frequency response analyses on dynamics of shifting and tilting DOFs in the next step.

3.1. Finite Element Analysis of Dynamics and Product Variability

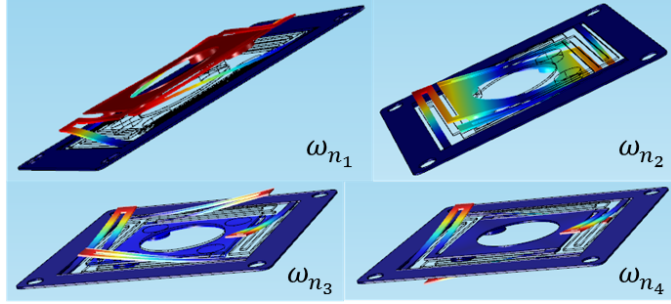
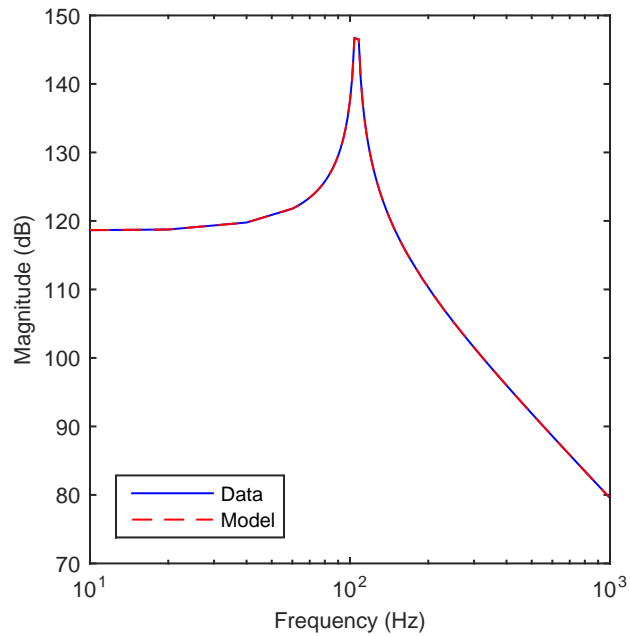


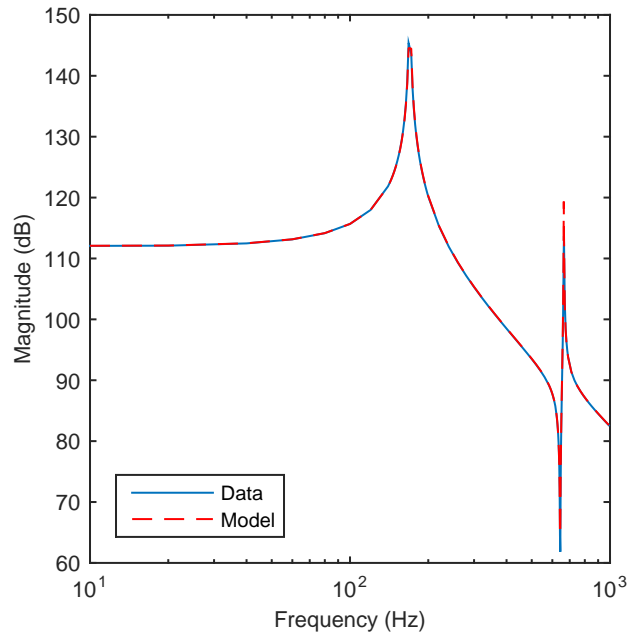
Figure 3.1: Eigen frequency analysis results

To identify dynamics of shifting and tilting DOFs, frequency response of lens-platform to translational and rotational actuation is obtained. In Figures 3.2(a) and 3.2(b), blue solid lines indicate frequency responses of shifting and tilting dynamics of OIS, respectively. Shifting dynamics only includes shifting mode, while tilting dynamics has tilting mode as well as 3rd and 4th modes. Dynamics of OIS is lightly-damped because of its low-friction mechanical design discussed in Section 2.1. The bandwidth of the tilting dynamics is 260 Hz which is sufficiently larger than the hand-shake disturbance bandwidth (20 Hz) shown in Figure B.2.

3.1. Finite Element Analysis of Dynamics and Product Variability



(a) Shifting dynamics



(b) Tilting dynamics

Figure 3.2: Nominal dynamics of OIS

3.2. Dynamic Uncertainty Modeling of OISs

Since the focus in OIS is the tilting, and not the shifting, effects of beam width variation and actuator imbalance are studied on tilting dynamics (Figure 3.2(b)). Figure 3.3 shows the results of this study where Figure 3.3(a) and Figure 3.3(b) show the tilting dynamics (Figure 3.2(b)) under perturbation of beam width and force imbalance, respectively. Figure 3.3(a) shows tilting frequency responses of OIS under $\pm 10\%$ beam width variations of the nominal width. Beam width variations lead to uncertainties in DC gain of tilting dynamics as well as all natural frequencies because the beam width is related to spring stiffness. To be more specific, the increase of beam width increases stiffness, leading to the decrease in DC gain and the increase in natural frequencies. Figure 3.3(b) shows tilting frequency response of OIS under $\pm 10\%$ imbalance in actuator forces. Force imbalance brings about coupling of shifting dynamics with tilting dynamics. As percentage of force imbalance increases, magnitude of coupling increases. The damping ratios do not change in either scenarios because they are affected by material of the lens-platform rather than its geometry.

3.2 Dynamic Uncertainty Modeling of OISs

The objective of dynamic uncertainty modeling is to develop a mathematical representation of the dynamic behaviour of the OIS as well as product variabilities based on FEA results presented in Section 3.1. According to Section 2.2, the model considers the torque generated on the lens-platform as control input and the tilt angle of the lens-platform as measured output. Based on FEA results, a linear model of the following structure is proposed:

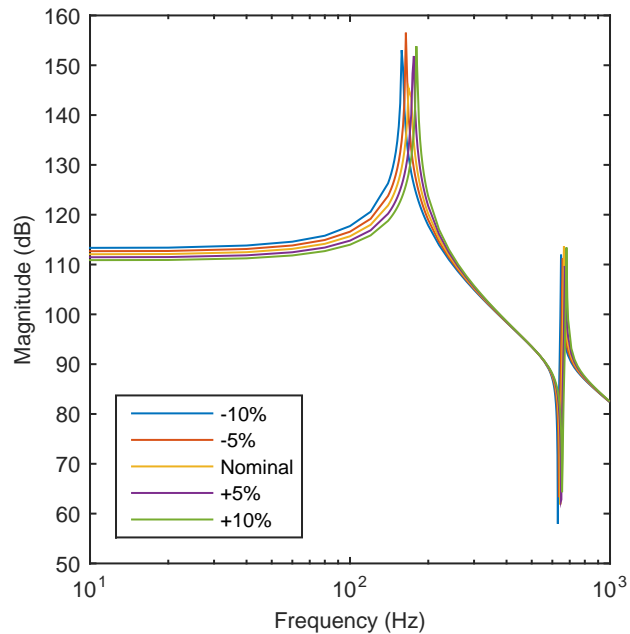
$$G(s, \delta) = [G_{shift}(s, \delta) + G_{tilt}(s, \delta)]e^{-s\tau}, \quad (3.1)$$

where G_{shift} and G_{tilt} denote the transfer functions corresponding to the coupling of shift dynamics and the tilt dynamics, respectively, and δ designates the uncertainty parameter vector representing product variabilities. For each of these terms, a linear model of following structure is proposed from Figure 3.2:

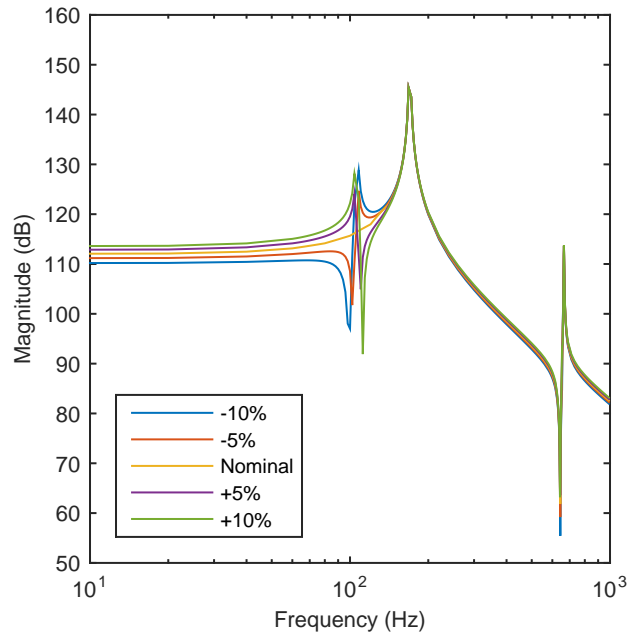
$$G_{shift}(s, \delta) = \frac{k_{shift}\omega_{n_1}^2}{s^2 + 2\xi_1\omega_{n_1}s + \omega_{n_1}^2}, \quad (3.2)$$

$$G_{tilt}(s, \delta) = \frac{k_{tilt}\omega_{n_2}^2}{s^2 + 2\xi_2\omega_{n_2}s + \omega_{n_2}^2} \cdot \frac{\frac{\omega_{n_4}^2}{s^2 + 2\xi_4\omega_{n_4}s + \omega_{n_4}^2}}{\frac{\omega_{n_3}^2}{s^2 + 2\xi_3\omega_{n_3}s + \omega_{n_3}^2}}, \quad (3.3)$$

3.2. Dynamic Uncertainty Modeling of OISs



(a) Beam width uncertainties



(b) Actuator installation uncertainties

Figure 3.3: Effect of uncertainties on tilting dynamics

3.2. Dynamic Uncertainty Modeling of OISs

where ω_{n_i} and ξ_i are respectively natural frequency and damping ratio of the i^{th} mode, K_{shift} is DC-gain of the coupling mode, and K_{tilt} denotes DC-gain of the tilt dynamics.

Product variabilities are represented by parametric uncertainties in model G . Based on FEA results, natural frequencies and DC-gains are considered uncertain while the damping ratios are assumed to be fixed. K_{shift} is considered as a standalone uncertainty parameter representing force imbalance (Figure 3.3(b)), while ω_{n_2} is the uncertainty parameter representing beam width variations (Figure 3.3(a)). Therefore, two independent uncertainty parameters are defined as

$$\delta = [k_{shift}, \omega_{n_2}]. \quad (3.4)$$

The independent uncertainty parameters vary between an upper-bound and lower-bound as follows:

$$\underline{k}_{shift} < k_{shift} < \overline{k}_{shift}, \underline{\omega}_{n_2} < \omega_{n_2} < \overline{\omega}_{n_2}, \quad (3.5)$$

where underline and overline represent respectively the lower-bound and upper-bound of each uncertainty parameter. The upper-bound and lower-bound values should be identified experimentally.

Uncertainties in $\omega_{n_i}, i = 1, 3, 4$, and k_{tilt} are considered to be correlated with ω_{n_2} because they are due to the same mechanical origin (beam width variations). Furthermore, this correlation leads to a control-oriented model that can be dealt with by the robust control theories introduced in Section 1.4.2 effectively. The correlations in all other parameters are defined as follows:

$$\omega_{n_i} = \omega_{n_i}^* \left(\frac{\omega_{n_2}}{\omega_{n_2}^*} \right)^{c_i}, i = 1, 3, 4, \quad (3.6)$$

$$k_{tilt} = k_{tilt}^* \left(\frac{\omega_{n_2}^*}{\omega_{n_2}} \right)^{2c_k}, \quad (3.7)$$

where the superscript * denotes the nominal values of dynamics parameters to be identified experimentally. These equations can be derived from fundamental equations $\omega_n = \sqrt{K/J}$ and $k = 1/K$ for a simple second-order mass-spring-damper system assuming only stiffness variations (beam width). Addition of correction factors $c_i, i = 1, 3, 4$ and c_k are added to account for the increased complexity of the OIS compared to a simple mass-spring-damper system.

3.3. Robust Controller Design for OISs

Based on independent uncertainty parameters k_{shift} and ω_{n_2} , the uncertainty region can be represented by a rectangle as illustrated in Figure 3.4. With this uncertainty region, two uncertainty models can be defined: real parametric uncertainty model $G(s, \delta)$ and multi-model $G_i(s) = D_{yu,i} + C_{y,i}(sI - A_i)^{-1}B_{u,i}, i = 1, 2, 3, 4$. The real parametric uncertainty model considers the area inside the rectangle while the multi-model uncertainty model only considers the vertices. In this thesis, the emphasis is put on multi-model uncertainty model to design the robust H_∞ controller described in the next section. The real parametric uncertainty model is merely used to design the μ -synthesis controller (introduced in Subsection 1.4.2) for comparison purposes.

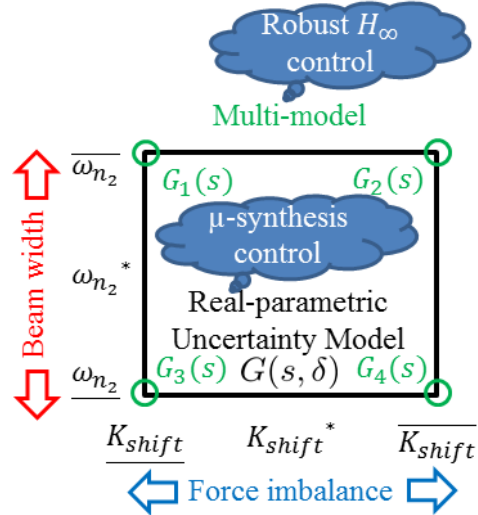


Figure 3.4: Illustration of uncertainty region and definitions of uncertainty models

3.3 Robust Controller Design for OISs

In this section a robust controller design method is developed to deal with the multi-model. The robust H_∞ controller design method is based on the theory published in [27]. This theory can consider uncertainties modeled in the previous section while providing the following additional advantages compared to conventional off-the-shelf robust control methods such as μ -synthesis:

3.3. Robust Controller Design for OISs

- The controller order is theoretically constrained by order of plant model. Therefore, arbitrarily low-order controller can be designed as opposed to μ -synthesis control theory.
- The robust controller design problem is formulated as an bilinear matrix inequality (BMI) optimization problem which can be solved using efficient algorithms.
- A systematic way of solving for a good initial guess for solution of the non-convex optimization problem that is critical for performance of the designed controller.
- Non-integer values for correction factors $c_i, i = 1, 3, 4$ and c_k (introduced in Equation 3.6 and Equation 3.7) are handled to reduce conservatism of the designed controller.

The robust control problem is illustrated in Figure 3.5 as a weighted control system block-diagram, where $K(s)$ and $G(s, \delta)$ denote the output-feedback robust H_∞ controller and a set of OISs, respectively. e is the tracking error, u is the control input (torque), and y is the measured output (tilt angle). r is an uncertain reference signal generated by the hand-shake signal, and δ is uncertainty parameter representing product variabilities. e_w and u_w are weighted tracking error and control input signals based on which the performance channel z is defined as follows:

$$z := [e_w \ u_w]^T \quad (3.8)$$

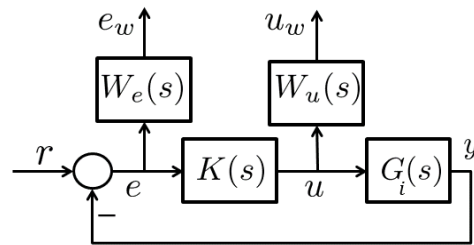


Figure 3.5: Weighted control system block-diagram

The state-space realization of the generalized plant corresponding to this

3.3. Robust Controller Design for OISs

weighted control system configuration is denoted as:

$$\begin{bmatrix} \dot{x} \\ z \\ y \end{bmatrix} = \begin{bmatrix} A_i & B_{r,i} & B_{u,i} \\ C_{z,i} & D_{zr,i} & D_{zu,i} \\ C_{y,i} & D_{yr,i} & D_{yu,i} \end{bmatrix} \begin{bmatrix} x \\ r \\ u \end{bmatrix} \quad (3.9)$$

The robust H_∞ controller design method guarantees robust closed-loop stability and performance by considering uncertainty parameter δ (C3). The weighting function W_e is used to penalize tracking error (O1), reduce steady-state error (S1), and meet stability margin specifications (S2). W_u is a weighting functions used to penalize control effort (O2) and avoid saturation due to noise amplification (S3). To avoid undue increase of controller order (O3), we propose using constant W_u and first order W_e parameterized as follows [70]:

$$W_e(s) = \frac{s/M_H + \omega_b}{s + \omega_b M_L}, \quad (3.10)$$

where M_L , M_H , and ω_b are design parameters which, respectively, denote low-frequency gain, high-frequency gain, and 0 dB crossing frequency of W^{-1} . To reduce steady state error (S1), M_L should be decreased. Tracking error (O1) can be reduced by increasing ω_b . To increase stability margin (S2), peak of sensitivity M_H should be reduced. Finally, W_u is taken as a constant gain, and it is increased to save control effort (O2) and avoid saturation due to noise amplification (S3).

Due to inherent trade-off between performance objectives and specifications, controller design parameters M_L , M_H , ω_b , and W_u are selected such that performance objectives improve while performance specifications are satisfied. To select the controller design parameters, trial-and-error is performed because there is no explicit relationship between the controller design parameters and the performance objectives and specifications to formulate and optimization problem.

The control problem is to find a robustly stabilizing controller parameter matrix Θ of form

$$\Theta = \begin{bmatrix} A_K & B_K \\ C_K & D_K \end{bmatrix} \quad (3.11)$$

that solves

$$\min_{\Theta} \max_i \|\mathcal{T}_{rz,i}(\Theta)\|_{\infty} \quad (3.12)$$

3.3. Robust Controller Design for OISs

where $\mathcal{T}_{rz,i}$ is the closed-loop system from r to z corresponding to $G_i(s)$ expressed as:

$$\mathcal{T}_{rz,i}(s) := \begin{bmatrix} A_{0,i} + \mathcal{B}_i \Theta \mathcal{C}_i & B_{0,i} + \mathcal{B}_i \Theta \mathcal{D}_{yr,i} \\ C_{0,i} + \mathcal{D}_{zu,i} \Theta \mathcal{C}_i & D_{yu,i} + \mathcal{D}_{zu,i} \Theta \mathcal{D}_{yr,i} \end{bmatrix} \quad (3.13)$$

where the matrices are defined as

$$A_{0,i} = \begin{bmatrix} A_i & 0 \\ 0 & 0 \end{bmatrix} \quad (3.14)$$

$$\mathcal{B}_i = \begin{bmatrix} 0 & B_{u,i} \\ I & 0 \end{bmatrix}, B_{0,i} = \begin{bmatrix} B_{r,i} \\ 0 \end{bmatrix} \quad (3.15)$$

$$\mathcal{C}_i = \begin{bmatrix} 0 & I \\ C_{y,i} & 0 \end{bmatrix}, \mathcal{D}_{yr,i} = \begin{bmatrix} 0 \\ D_{yr,i} \end{bmatrix} \quad (3.16)$$

$$C_{0,i} = [C_{z,i} \ 0], \mathcal{D}_{zu,i} = [0 \ D_{zu,i}] \quad (3.17)$$

By applying the bounded real lemma to 3.13, this problem can be formulated as the following optimization problem [17]:

$$\min_{\Theta, P_i} \gamma \quad (3.18)$$

$$s.t. \Psi_i(P_i, \gamma) + \mathcal{Q}_i^T \Theta^T \mathcal{P}_i(P_i) + \mathcal{P}_i(P_i)^T \Theta \mathcal{Q}_i < 0 \quad (3.19)$$

where $P_i > 0$ is the closed-loop Lyapunov parameter matrix and matrices and other matrices can be written as:

$$\Psi_i(P_i, \gamma) = \begin{bmatrix} A_{0,i}^T P_i + P_i A_{0,i} & P_i B_{0,i} & C_{0,i}^T \\ * & -\gamma I & D_{zr,i}^T \\ * & * & -\gamma I \end{bmatrix} \quad (3.20)$$

$$\mathcal{P}_i(P_i) = [\mathcal{B}^T P_i \ 0 \ \mathcal{D}_{zu,i}^T] \quad (3.21)$$

$$\mathcal{Q}_i = [\mathcal{C} \ \mathcal{D}_{yr,i}^T \ 0] \quad (3.22)$$

In above equations, Ψ_i are affine with respect to P_i and γ , \mathcal{P}_i are affine with respect to P_i , and \mathcal{Q}_i are constant matrices merely dependent on system parameters (see [17] for derivations). Therefore, even though the problem is non-convex due to coupling of P_i and Θ ; it is convex with respect to either P_i and Θ individually. Using this properties, a sequential design procedure is employed to solve for a local optimum as follows:

3.3. Robust Controller Design for OISs

- 1 Employ the procedure proposed in [27] to solve for an initial feasible solution. Set the result of this procedure as Θ_1 and set $k = 1$.
- 2 Set $\Theta := \Theta_k$ and solve the convex problem 3.18 with respect to γ and P . Denote the solution for γ and P_i as γ_k and $P_{i,k}$, respectively.
- 3 Set $P_i := P_{i,k}$ and solve the convex problem 3.18 with respect to γ and Θ . Denote the solution for γ and Θ as γ_{k+1} and Θ_{k+1} , respectively.
- 4 If $\gamma_k - \gamma_{k+1} < \epsilon$, set $k := k + 1$ and go to step 2; otherwise, Θ_{k+1} is the parameter matrix of the designed controller.

In this section we present the procedure used for design of initially-feasible controller as the initial guess to solve the non-convex optimization problem (3.18) based on the method proposed in [27]. The procedure involves two steps corresponding to design of state-feedback and initially-feasible output-feedback controller as follows.

3.3.1 State-feedback Controller Design

In this subsection, the objective is to design a state-feedback controller C_K for multi-model (3.9) such that it stabilizes the closed-loop system and optimizes the robust H_∞ performance

$$\max_i \|\mathcal{T}_{rz,i}(C_K)\|_\infty \quad (3.23)$$

Theorem 6 in [27] states that this problem can be formulated as a convex optimization problem based on LMIs:

$$\min_{L,Q} \gamma, \ s.t. \begin{bmatrix} -\mathbb{A}_i - \mathbb{A}_i^T & B_{r,i} & \mathbb{C}_i^T \\ * & I & D_{zr,i}^T \\ * & * & \gamma I \end{bmatrix} < 0 \quad (3.24)$$

where $\mathbb{A}_i := A_i Q + B_{u,i} L$, $\mathbb{C}_i := C_{z,i} Q + D_{zu,i} L$, and $Q > 0$. Using the solutions L and Q , the optimal state-feedback controller is given as $C_K = LQ^{-1}$.

3.3.2 Output-feedback Controller Design

To design the initially-feasible output-feedback controller, the designed state-feedback controller is set for C_K and $D_K = 0$ in (3.11). By doing this,

3.4. Simulation Results

problem (3.13) is formulated as a convex problem based on LMIs (Theorem 8 in [27]):

$$\min_{L,Q} \gamma, \text{ s.t. } \begin{bmatrix} -M_i - M_i^T & N_i & \Omega_i^T \\ * & I & D_{zr,i}^T \\ * & * & \gamma I \end{bmatrix} < 0 \quad (3.25)$$

where

$$M_i := \begin{bmatrix} X_i(A_i + B_{u,i}C_K) & -X_iB_{u,i}C_K \\ Y(A_i + B_{u,i}C_K) - Z - G(C_{y,i} + D_{yu,i}C_K) & Z + GD_{yu,i}F - YB_{u,i}C_K \end{bmatrix}, \quad (3.26)$$

$$N_i := \begin{bmatrix} X_iB_{r,i} \\ YB_{r,i} - GD_{yr,i} \end{bmatrix} \quad (3.27)$$

$X_i, Y > 0$ and $\Omega_i := [C_{z,i} + D_{zu,i}C_K \quad -D_{zu,i}C_K]$. Using the solutions Z , G , and Y , controller parameters can be obtained as $A_K = Y^{-1}Z$ and $B_K = Y^{-1}G$.

3.4 Simulation Results

To preliminarily validate the proposed method, simulation studies are conducted. To this goal, first the proposed uncertainty model is validated by comparing model samples with FEA samples. Then a controller is designed based on the uncertainty model and its performance is compared to some baseline controllers in time-domain and frequency-domain.

3.4.1 Modeling, Validation, and Robust Controller Design

The parameters of the model (3.1) are obtained based on FEA results. The numeric values of the model parameters are listed in the first column of Table C.1. The model is validated in two stages: validation of nominal model structure and validation of uncertainty model structure. To validate model structure (3.1), nominal frequency responses of linear model and FEA are compared in Figure 3.2. As shown, the proposed model structure decently describes dynamics of the system.

To validate uncertainty modeling, samples of frequency response obtained by varying K_{shift} and ω_{n_2} in uncertainty model are compared with samples of frequency response obtained by varying force imbalance and beam

3.4. Simulation Results

width in FEA model, respectively. The results of uncertainty model validation are presented in Figure 3.6.

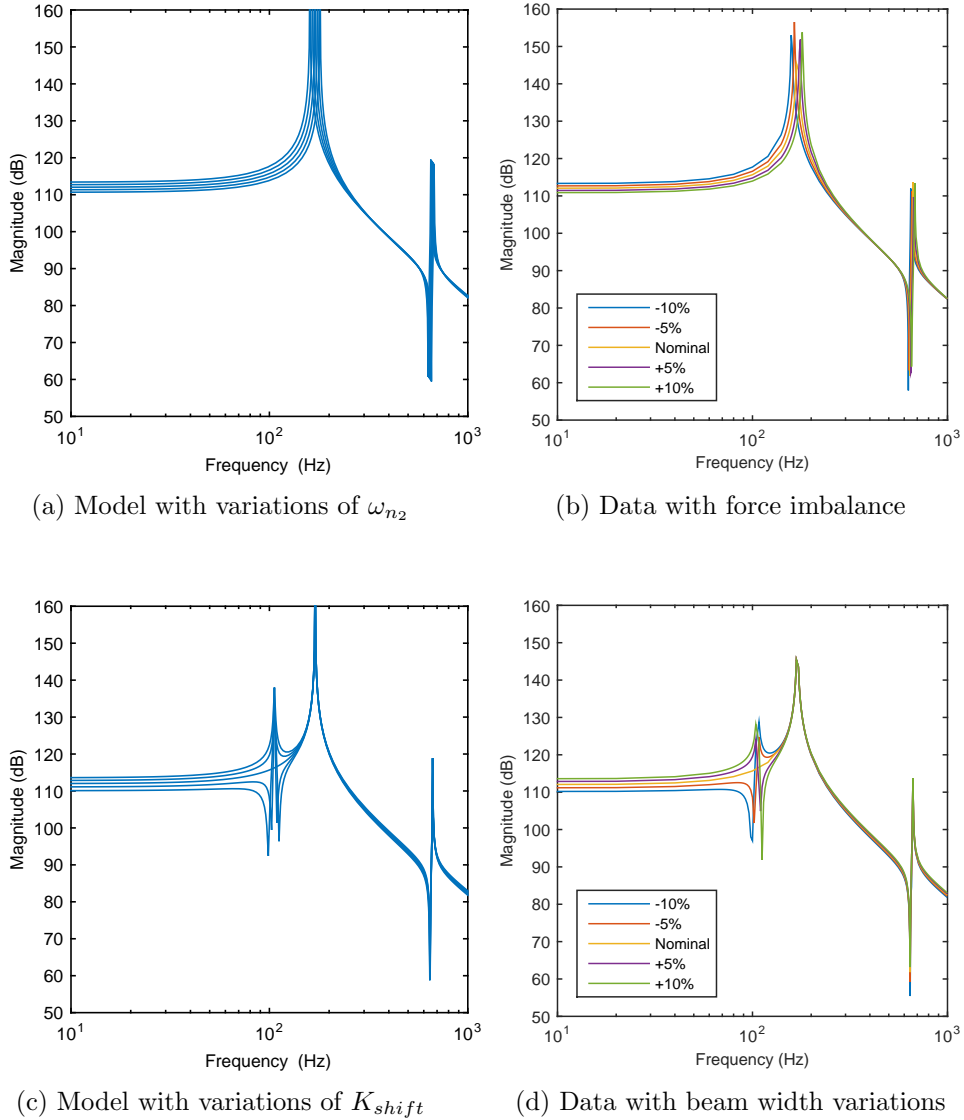


Figure 3.6: Model validation

In this figure, Figures 3.6(a) and 3.6(c) are samples of uncertainty model

3.4. Simulation Results

when ω_{n_2} and K_{shift} are perturbed, respectively, while Figures 3.6(b) and 3.6(d) are samples of FEA model when beam width and force imbalance are perturbed, respectively. By comparing these samples, it can be seen that uncertainties in K_{shift} and ω_{n_2} represent force imbalance and beam width variation, respectively.

The multi-model uncertainty model obtained based on these parameter values are compared with the combination of FEA data in Figure 3.7. The multi-model uncertainty model successfully captures the variations of frequency responses. A robust H_∞ controller is designed based on the multi-model uncertainty model. The controller design parameters (introduced in Figure 3.5 and Equation 3.10) for the robust H_∞ controller are listed in the first column of Table A.7.

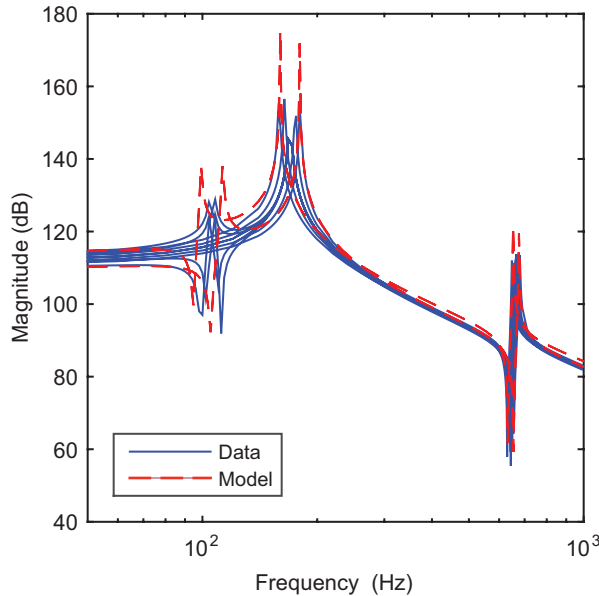


Figure 3.7: Multi-model dynamic uncertainty model for FEA model of miniaturized OIS

3.4.2 Closed-loop Stability Analysis of Model Samples

The designed robust H_∞ controller was compared with μ -synthesis controller and four nominal controllers, namely PID, lead-lag, LQG, and H_∞ controllers. The robust H_∞ controller is designed based on multi-model,

3.4. Simulation Results

whereas μ -synthesis controller is designed based on real-parametric uncertainty model. The nominal controllers are designed for the nominal plant model ($K_s = 0$ and $\omega_{n_t} = 453 \text{ Hz}$). The closed-loop system corresponding to different controllers is analyzed for different values of uncertainty parameters in the uncertainty region 3.5. The design parameters for these controllers are listed in Table A.2–A.7.

Figure 3.8 shows the analysis results. The closed-loop stability of PID, lead-lag, LQG, and H_∞ are illustrated in Figure 3.8(a), Figure 3.8(b), Figure 3.8(c), Figure 3.8(d), respectively. In these figures, the green circle mark and the red cross mark indicate that the closed-loop system is stable and unstable, respectively.

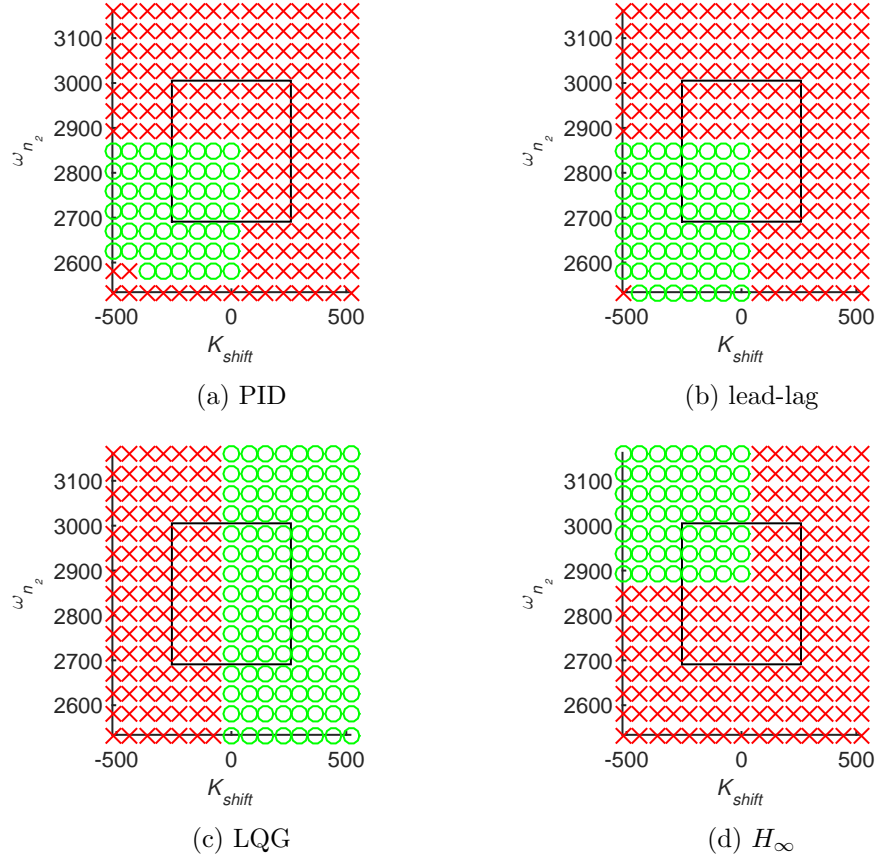


Figure 3.8: Analysis of robust closed-loop stability of conventional controllers on OIS model samples

3.4. Simulation Results

As shown, different nominal controllers can stabilize different subregions of the uncertainty region including the nominal plant model; however, none of them are capable of stabilizing the closed-loop system for the entire uncertainty region due to model-plant mismatch (C3). This is because the nominal controller design methods do not take uncertainties into account. On the other hand, both robust controllers (robust H_∞ controller and μ -synthesis controller) successfully stabilized the closed-loop system for the entire uncertainty region because they guarantee robust closed-loop stability in design stage.

3.4.3 Time- and Frequency-domain Performance Analysis

Time-domain performance is assessed by calculating root mean square (RMS) values of the tracking error signals. A set of tracking error signals are obtained for three cases corresponding to variabilities in beam width, force imbalances, and hand-shake disturbances. For each case, mean and worst-case of RMS values of the corresponding set is calculated. Figure 3.9 compares time-domain performance of different controllers, where the solid bars show the mean and the upper limit of the error bars show the worst-cases. In the figure, nominal controllers are de-tuned versions of controllers in Figure 3.8 to recover robust stability for uncertainty region (3.5).

3.4. Simulation Results

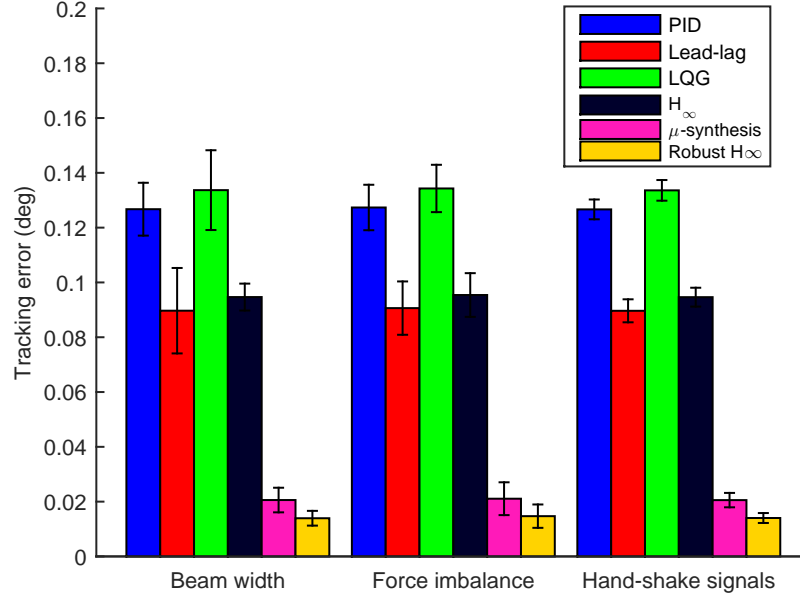


Figure 3.9: Time-domain performance assessment of different controllers on model samples of miniaturized OISs

As shown, the robust controller reduces the mean value of tracking error as well as its degradation (C1) compared to nominal controllers because it systematically optimizes the performance by considering uncertainties and utilizing optimization tools in design. This improvement is shown in three cases corresponding to variabilities in beam width, force imbalances, and hand-shake disturbances. More specifically, analysis shows that hand-shake disturbances could be suppressed about 44% better than average of nominal controllers.

Figure 3.10 demonstrates time-domain hand-shake suppression. In this figure, the black solid line is the plot of a real hand-shake signal collected by a mobile phone device. The blue dashed line and red dash-dot line are tracking error signals of the PID controller and the robust H_{∞} controller, respectively. As can be seen, the robust H_{∞} controller suppresses hand-shake disturbance more effectively than the PID controller does.

3.4. Simulation Results

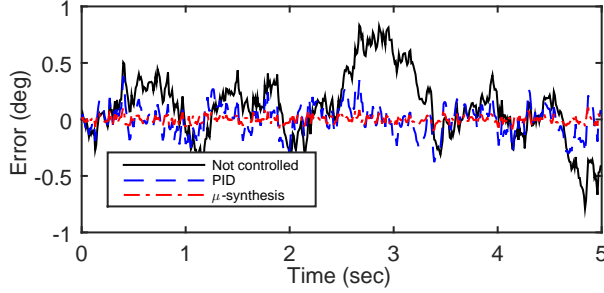


Figure 3.10: Comparison of hand-shake disturbance suppression of the robust H_∞ controller with the PID controller in time-domain

The robust H_∞ controller is compared with μ -synthesis controller more carefully because both of them are robust controllers that achieve robust closed-loop stability and optimized closed-loop performance. These controllers are compared in terms of controller order, tracking error, and control effort both in frequency-domain and time-domains.

Table 3.1 compares the robust H_∞ controller with the μ -synthesis controller. The robust H_∞ controller offers much lower controller order than the μ -synthesis controller does (C4) because it mathematically constraints the controller order. In Table 3.1, the values outside parenthesis for tracking error and control effort are mean values, while the ones inside parenthesis are the worst-case degradations. The robust H_∞ controller improves the mean (C1) and degradation (C3) of the tracking error as well as the mean value (C2) and degradation (C3) of the control effort compared to the μ -synthesis controller.

Table 3.1: Summary comparison of μ -synthesis with Robust H_∞ on miniaturized OIS simulation model samples

	μ -synthesis	Robust H_∞
Controller order (-)	68	11
Tracking error (deg)	0.0188 (0.0044)	0.0128 (0.0034)
Control effort (mAh)	0.1711 (0.0504)	0.1537 (0.0406)
Computation time (s)	43	201

Figure 3.11 and Figure 3.12 compares the robust H_∞ controller with the μ -synthesis controller in terms of the magnitude Bode plot of the transfer functions from r to e and from r to u , respectively. As shown in Figure 3.11,

3.4. Simulation Results

the robust H_∞ controller has better error rejection than the μ -synthesis controller (C1). More specifically, 0 dB crossing frequency is 42 Hz for robust H_∞ controller, while the one for μ -synthesis controller is 38 Hz.

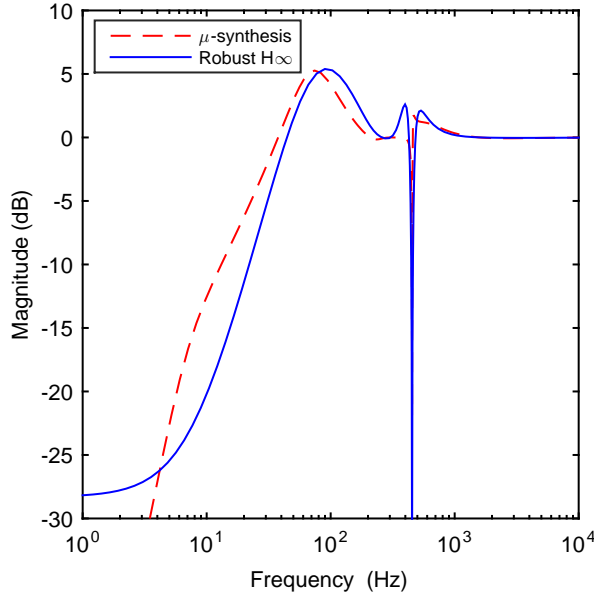


Figure 3.11: Frequency response of transfer function from reference to tracking error on nominal model

In Figure 3.12, the robust H_∞ controller uses less control effort (C2) compared to the μ -synthesis controller in low-frequency band. The improvements achieved in tracking error and control effort can be associated with the ability of the proposed robust H_∞ controller design method to systematically generate decent initial guess for solution of the optimization problem corresponding to the proposed controller design problem, and to handle non-integer correction factors in the proposed uncertainty model. On the other hand, the computation time for design of the robust H_∞ controller is slightly longer than that for the μ -synthesis controller because the μ -synthesis controller is designed using numerically-optimized off-the-shelf algorithms while custom-made algorithms are developed and used for design of the robust H_∞ controller.

3.4. Simulation Results

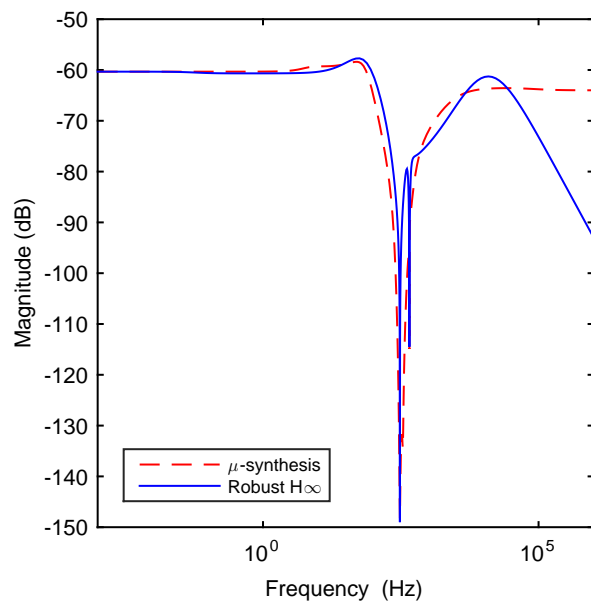


Figure 3.12: Frequency response of transfer function from reference to control input on nominal model

Chapter 4

Experimental Results

4.1 Experimental Setups

This chapter presents the experimental results. The experimental results include detailed explanation of the experimental setups and methodologies used for conducting experiments. Then, same setups and methodologies are used to implement the proposed method on large-scale (Section 4.3) and miniaturized (Section 4.4) OISs and assess the results. The experimental setups are two folds: open-loop and closed-loop. The open-loop setup is for system identification and is presented in Section 4.1.1. The closed-loop setups are for controller implementation and assessments performed in time-domain (Section 4.1.2) and frequency-domains (Section 4.1.3). The equipment used in these experimental setups are shown in Figure 4.1. The experimental setups include a dynamic signal analyser (DSA) (not shown in Figure 4.1), a digital signal processor (DSP), an amplifier, an OIS (plant), and a laser Doppler vibrometer (LDV).

4.1.1 Open-loop Frequency-domian System Identification

In this subsection, the procedure and experimental setup used for frequency-domain system identification of OISs are described in details. The data obtained from this setup is used for parameter identification of the dynamic uncertainty model (3.1). More specifically, the objective is to identify nominal dynamics parameters in (3.1) (k_{tilt}^* , $\omega_{n_i}^*$, ξ_i , $i = 1, \dots, 4$) and bounds on uncertainties in (3.5) (\underline{k}_{shift} , \overline{k}_{shift} , $\underline{\omega}_{n_2}$, $\overline{\omega}_{n_2}$).

Figure 4.2 shows connection of equipments for open-loop frequency-domian system identification. The dynamic signal analyzer generates sinusoidal analog control input signals that are passed to the digital signal processor for signal processing. Then, the output of the digital signal processor is passed to an amplifier that generates sufficient current to be applied to coils of the OIS. The tilt angle of the OIS is measured using laser Doppler Vibrometer and fed back to the dynamic signal analyzer for analysis. The dynamic signal analyzer calculates frequency response data based on its in-

4.1. Experimental Setups

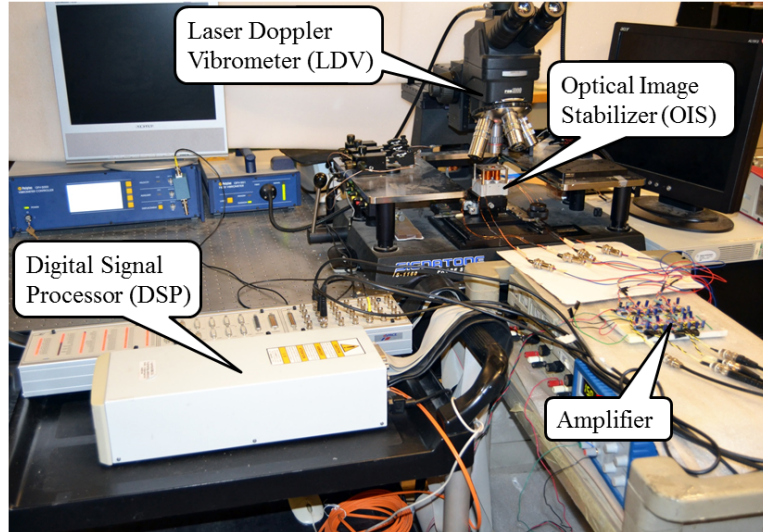


Figure 4.1: The experimental setup

put and output signals. According to specifications, the LDV has 320 nm resolution, 20 kHz bandwidth which is sufficient to accurately characterize dynamics of the system in high-frequency band.

The output frequency response data from this procedure characterizes $k_{tilt}^*, \omega_{n_i}^*, \xi_i, i = 1, \dots, 4$. Re-iteration of this procedure for different OISs generates a data set that characterizes $k_{shift}, \bar{k}_{shift}, \underline{\omega_{n_2}}, \bar{\omega_{n_2}}$.

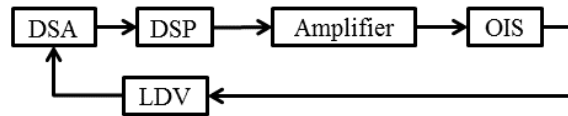


Figure 4.2: Open-loop frequency-domain system identification setup

4.1.2 Closed-loop Time-domain Controller Implementation

In this subsection, the procedure and experimental setup used for closed-loop time-domain implementation of the designed controllers are described in detail. The data from this setup is used for assessment of closed-loop performance of controllers in time-domain.

Figure 4.3 shows connection of equipments for closed-loop time-domain controller implementation. The digital signal processor is used to apply

4.1. Experimental Setups

negative of the hand-shake signals (described in Appendix B) as reference signal. The actual tilt angle of the OIS is measured by the laser Doppler vibrometer and subtracted from the reference signal. The resulting error signal is passed to the designed controller implemented on dSPACE digital signal processor. The command control input generated by the designed controller is passed to an amplifier that generates sufficient current to be applied to coils of the OIS. The tilt angle of the OIS is measured using laser Doppler Vibrometer and fed back.

The measurement signals of the laser Doppler vibrometer and currents applied to coils are logged to analyze the tracking error (e) and control effort (i_k , $k = 1, \dots, 4$) for assessment purposes.

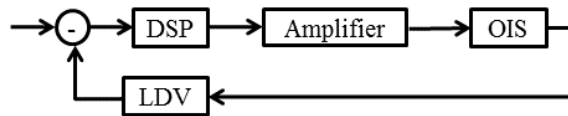


Figure 4.3: Closed-loop time-domain controller implementation setup

4.1.3 Closed-loop Frequency-domian System Identification

In this subsection, the procedure and experimental setup used for identification of the closed-loop in frequency-domain are described in details. The data from this setup is used for assessment of closed-loop performance of controllers in frequency-domain.

Figure 4.4 shows connection of the equipments for closed-loop frequency-domian system identification. The dynamic signal analyzer generates sinusoidal analog reference signal r . The actual tilt angle of the OIS is measured by the laser Doppler vibrometer and subtracted from the reference signal. The resulting error signal is passed to the designed controller implemented on dSPACE digital signal processor. The command control input generated by the designed controller is passed to an amplifier that generates sufficient current to be applied to coils of the OIS. The tilt angle of the OIS is measured using laser Doppler Vibrometer and fed back to the dynamic signal analyzer for analysis. The dynamic signal analyzer calculates frequency response data based on its input and output signals.

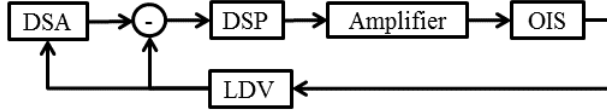


Figure 4.4: Closed-loop time-domain controller implementation setup

4.2 Experimental Methodologies

This subsection presents the methodologies used for performing experiments and analysing experimental results. These methodologies are similarly used for application of the proposed method to large-scale and miniaturized OISs presented in the following sections. Experimental methodologies associated with four tests are explained: system identification tests, closed-loop stability tests, time-domain tests, and frequency-domain tests. These explanations includes the objectives of the tests, the experimental setups used in the tests, parameter settings of different equipments in the setups, parameters changed during the experiments, and how the experimental data are analysed, interpreted, and compared.

4.2.1 System Identification Tests

The system identification tests are used to obtain the frequency response database in Figure 1.9. The frequency response database is obtained by measuring frequency response of 5 physical OIS prototypes that represent samples collected from the OIS production line in Figure 1.9. The frequency responses are measured using the open-loop frequency-domain system identification setup introduced in Section 4.1.1. The frequency response database is used to identify the parameters of model (3.1).

4.2.2 Closed-loop Stability Tests

The closed-loop stability tests check the closed-loop stability of a controller for perturbed OIS prototypes. The controllers participating in the experiment are the proposed robust H_∞ controller, μ -synthesis controller, and four conventional nominal controllers, namely PID, lead-lag, LQG, and H_∞ controllers. The robust H_∞ controller is designed based on multi-model uncertainty model, the μ -synthesis controller is designed based on real-parametric uncertainty model, and all nominal controllers are designed for OIS 3. The design parameters for these controllers are listed in Table A.2–A.7. The

4.2. Experimental Methodologies

controllers are implemented in the closed-loop time-domain controller implementation setup introduced in Section 4.1.2.

4.2.3 Time-domain Performance Tests

The time-domain performance tests are conducted to assess the tracking error, the control effort, and their degradation with uncertainties for the controllers mentioned in previous subsection. To this goal, the nominal controllers designed for closed-loop stability tests are de-tuned such that they recover closed-loop stability for the uncertainty region (3.5). To de-tune, a design parameter that best represents trade-off of closed-loop performance and robustness in each controller design method (such as proportional gain in classical controller design methods) is adjusted in the corresponding controller designed for OIS 3 to increase robustness such that the controller would stabilize the closed-loop system for the entire uncertainty region. The design parameters of the de-tuned controllers are listed in Tables A.2–A.5 in parenthesis next to the controller designs parameters corresponding to the nominal controllers.

These de-tuned controllers as well as the robust controllers are implemented in the closed-loop time-domain controller implementation setup introduced in Section 4.1.2. In the setup, each controller is tested 25 times with 5 OIS prototypes 5 hand-shake disturbance signals and the corresponding tracking error and control input signals are measured. The results are analysed for three cases. In each case, a certain combination of the OISs and the hand-shake disturbance signals are used, then the mean value and the worst-case value of the performance measure is calculated. The combination of the OISs and hand-shake disturbance signals used for each case are explained below:

- Case 1 In this case, OIS 3 is used subject to the hand-shake disturbance signals 1-5 to assess the robustness of the closed-loop performance to uncertainties in the hand-shake disturbance signals.
- Case 2 In case 2, OISs 1-5 are used subject to hand-shake disturbance signal 1 to assess the robustness of the closed-loop performance to uncertainties in the OIS dynamics.
- Case 3 In this case, OISs 1-5 is used subject to the hand-shake disturbance signals 1-5 and the overall performance is analyzed to assess the overall robustness of the closed-loop performance.

4.3. Application to Large-scale OIS prototypes

The performance measure for the tracking error is chosen as the RMS value of the tracking error signal in degrees (deg), while the performance measure for the control effort is chosen as the integral of the absolute current values over time in milli-ampere hour (mAh).

4.2.4 Frequency-domain Performance Test

The frequency-domain performance tests are performed to compare closed-loop performance of the designed robust controllers with more details and to validate their time-domain performance results. To this goal, the designed robust controllers are implemented in the closed-loop frequency-domain system identification setup (introduced in Section 4.1.3) including OIS 3. The frequency responses from r to e and from r to u (in Figure 3.5) are measured to evaluate tracking error and control effort.

4.3 Application to Large-scale OIS prototypes

The proposed method is experimentally validated on stand-alone prototypes (rather than OISs integrated with a mobile phone device) because there are not available mobile phone devices designed to incorporate a lens-tilting OIS, nor there are any detailed design of this conceptual design in the literature that focuses on implementation on a mobile phone camera. The objective of implementation of the proposed method on large-scale OIS prototypes is to demonstrate feasibility of the method in an experimental setting and its capability to deal with physical product variabilities. To achieve this goal, OIS prototypes are built in large-scale for practical fabrication by available general-purpose prototyping facilities. Section 4.3.1 describes details of the large-scale prototypes used in these experiments. In Section 4.3.2, the application of the proposed method to the large-scale OIS prototypes are explained. Finally, experimental methodologies (introduced in Section 4.2) are used to obtain experimental results in Section 4.3.3.

4.3.1 Large-scale OIS Prototypes

In this subsection, details of the large-scale prototypes used in the experiments of this section are explained. The explanations include the mechanical design details, the product variabilities in large-scale OISs, and the system identification results obtained by implementation of system identification tests (introduced in Section 4.2.1) on large-scale prototypes.

4.3. Application to Large-scale OIS prototypes

Figure 4.5 shows a large-scale OIS prototype. The prototype is scaled about 5 times. The lens platforms are made of 17-7 stainless steel and fabricated using a water-jet cutter. The lens platform is installed on an aluminium base with screws. The coils are custom-made with copper wires wound around a core. The material of the core is copper, which has almost the same permeability as air. So the coil can be considered as a air-core coil. The number of turns for one of the four coils are counted and the number of turns of others are estimated based on the number of the layers and the number of turns in one layer. The permanent magnets are commercial rare-earth magnets attached to the lens platform by magnetic force. The numeric values for design parameters of the moving magnet actuators are tabulated in the second column of Table C.2 in Appendix C.

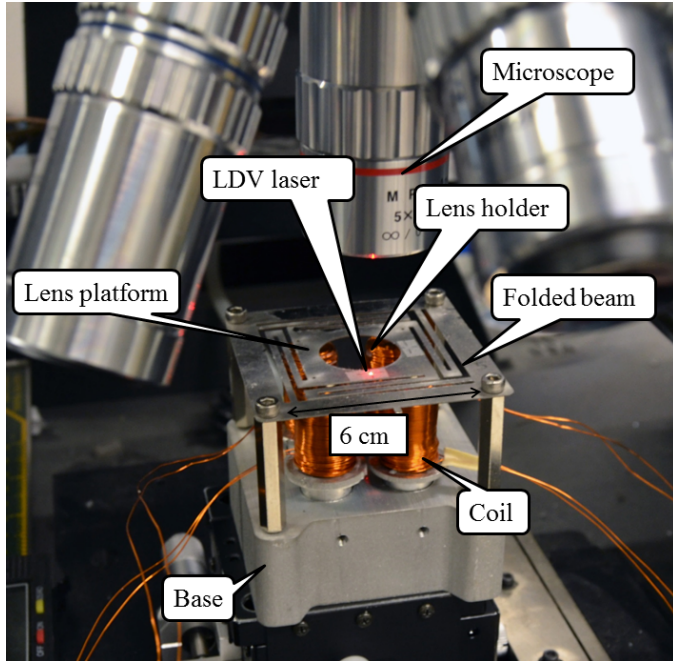


Figure 4.5: Large-scale OIS prototype

To mimic product variabilities in the miniaturized OISs, 5 lens platforms are fabricated with synthetic errors of -10%, -5%, 0%, 5%, and 10% in beam width as shown in Figure 4.6. The prototypes generated by assembling each of these lens platform on the base (shown in Figure 4.5) are referred to as OIS 1, OIS 2, OIS 3, OIS 4, and OIS 5, respectively.

The system identification tests (described in Section 4.2.1) are performed

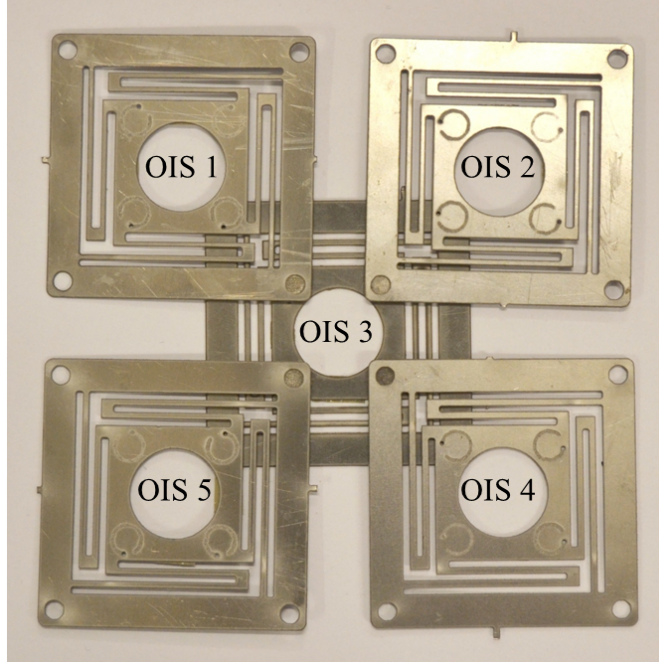


Figure 4.6: Product variabilities in large-scale lens platforms

on the large-scale prototypes. Figure 4.7 shows the frequency responses of OIS 1–OIS 5. The line colors in this figure are chosen correspondingly with simulation results in Figure 3.3(a). In general the structure of the experimental frequency responses are similar to simulation ones because conceptual design is the same. The bandwidth is reduced to about 150 Hz due to scaling; however, it is still sufficiently larger than the hand-shake disturbance bandwidth (20 Hz) shown in Figure B.2. In Figure 4.7, uncertainties in natural frequencies and DC gain can be observed. These uncertainties are due to beam width variations. As can be seen, with an increase in beam width from OIS 1 to OIS 5, the natural frequencies increase and DC gains decrease. In addition, the coupling of shifting mode due to force imbalance in simulations (Figure 3.3(b)) appears around 60 Hz in Figure 4.7 due to asymmetric actuation.

4.3.2 Robust Control of Large-scale OIS Prototypes

This subsection explains the application of the proposed method in Chapter 3 to the large-scale OIS prototypes introduced in the previous subsec-

4.3. Application to Large-scale OIS prototypes

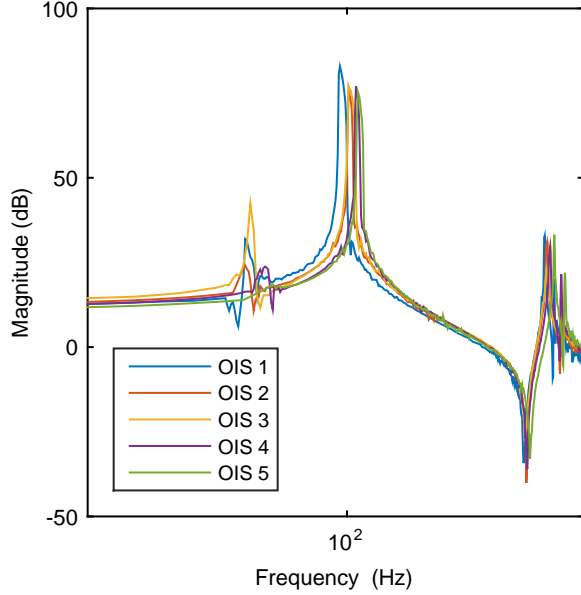


Figure 4.7: Frequency responses of large-scale OISs

tion. This explanation includes dynamic uncertainty modelling (introduced in Section 3.2) and robust H_∞ controller design (introduced in Section 3.3) for large-scale OIS prototypes.

The parameters of the model (3.1) are obtained based on the system identification results. The numeric values of the model parameters are listed in the second column of the Table C.1. The multi-model uncertainty model obtained based on these parameter values are compared with the system identification results in Figure 4.8. The multi-model uncertainty model successfully captures the variations of frequency responses. A robust H_∞ controller is designed based on the multi-model uncertainty model. The controller design parameters (introduced in Figure 3.5 and Equation 3.10) for the robust H_∞ controller are listed in the second column of Table A.7.

4.3.3 Assessments of Robustness for Closed-loop Stability and Performance

In this subsection, the experimental methodologies introduced in Section 4.2 are applied to the large-scale OIS prototypes described in Section 4.3.1.

4.3. Application to Large-scale OIS prototypes

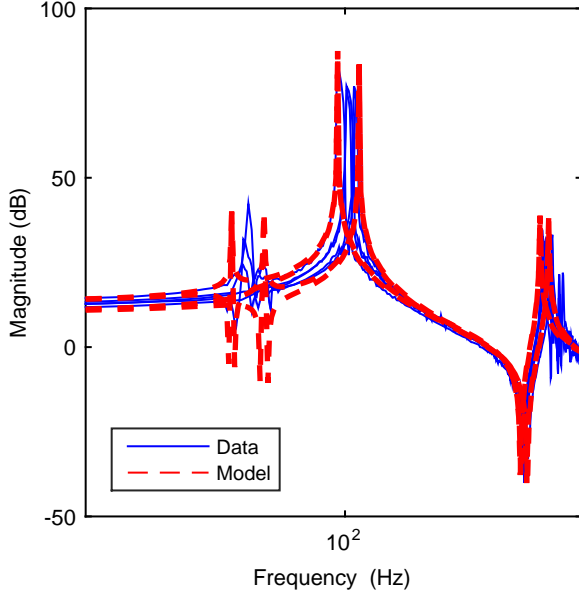


Figure 4.8: Multi-model dynamic uncertainty model of large-scale OIS

More specifically, this subsection includes results obtained from implementation of closed-loop stability, time-domain, and frequency-domain tests that were discussed in Section 4.2.2-4.2.4 of Section 4.2.

Table 4.1 shows the results for the closed-loop stability tests. In this experiment, the designed controllers in each row are implemented on different prototypes in each column. If the closed-loop system corresponding to the controller and the prototype was stable, the cell at intersection of the row associated with the controller and the column associated with the prototype is designated by a check mark (✓), otherwise it is designated by a cross mark (✗) is used to show that the closed-loop system was unstable. According to Table 4.1, None of nominal controllers can stabilize the closed-loop system corresponding to all OISs because the nominal controller design methods do not take uncertainties into account. On the other hand, both robust controllers (robust H_∞ controller and μ -synthesis controller) stabilized the closed-loop system for all prototypes (C3) because the robust controller design methods take uncertainties into account and guarantees robust closed-loop stability against uncertainties in the design stage.

Figure 4.9 illustrates the results of time-domain performance tests. In

4.3. Application to Large-scale OIS prototypes

Table 4.1: Assessment of closed-loop stability robustness in large-scale OISs

	OIS 1	OIS 2	OIS 3	OIS 4	OIS 5
PID	✗	✗	✓	✓	✓
lead-lag	✗	✗	✓	✓	✓
LQG	✓	✓	✓	✗	✗
H_∞	✗	✗	✓	✓	✓
μ -synthesis	✓	✓	✓	✓	✓
Robust H_∞	✓	✓	✓	✓	✓

the bar diagrams, the solid bars indicates the mean values of the RMS error while the upper limit of error bars denote the worst-case RMS error. The results are consistent with simulation results (Figure 3.9). The robust controllers reduce the mean values (C1) and degradation of tracking error (C3) compared to nominal controllers because the robust controller design methods take uncertainties into account and systematically optimize robust closed-loop performance against uncertainties to minimize conservatism. This improvement is shown against variations in hand-shake signals, OIS uncertainties, and both. The improvements are slightly less than improvements achieved in simulations. More specifically, analysis shows that hand-shake disturbances can be suppressed about 41% better than average of nominal controllers.

The robust H_∞ controller is compared with μ -synthesis controller more carefully because both of them are robust controllers that achieve robust closed-loop stability and optimized closed-loop performance. These controllers are compared in terms of controller order, tracking error, and control effort both in frequency-domain and time-domains.

Table 4.2 summarizes comparison of the robust H_∞ controller with the μ -synthesis controller. The controller order for robust H_∞ controller is much smaller than that of the μ -synthesis controller (C4) because the robust H_∞ controller design method mathematically constraints the controller order. The reduction in controller order is comparable with simulation results. The controller order reduction is performed by standard model reduction techniques. The controller order is reduced as long as closed-loop stability and closed-loop performance specifications are not violated for the entire uncertainty region (3.5). Then, the tracking error and control effort measurements are performed based on the reduced order controller. For tracking error and control effort, the values outside parenthesis are mean values, while the ones

4.3. Application to Large-scale OIS prototypes

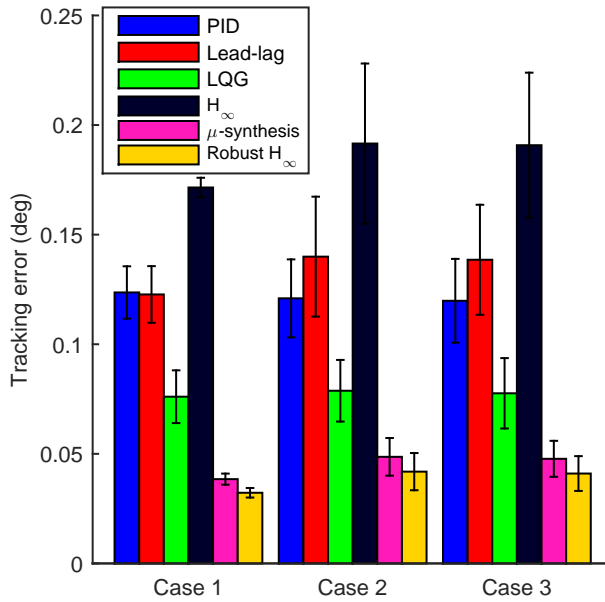


Figure 4.9: Time-domain performance assessment of different controllers on large-scale OISs

inside parenthesis are the worst-case degradations. The robust H_{∞} controller reduces mean (C1) and degradation (C3) of the tracking error as well as the mean (C2) and the degradation (C3) of the control effort compared to the μ -synthesis controller. The improvements achieved in large-scale experiments are similar to improvements achieved in simulations; however, the tracking errors are all higher compared to simulation because more stability margin was necessary to account for modeling errors in an experimental setting.

4.3. Application to Large-scale OIS prototypes

Table 4.2: Summary comparison of μ -synthesis with Robust H_∞ on large-scale OISs

	μ -synthesis	Robust H_∞
Designed order (-)	76	11
Reduced order (-)	18	9
Tracking error (deg)	0.0451 (0.0082)	0.0385 (0.0079)
Control effort (mAh)	0.4556 (0.1153)	0.4555 (0.1152)
Computation time (s)	75	269

Figure 4.10 and Figure 4.11 show the results of the frequency-domain performance tests. Figure 4.10 and Figure 4.11 compares the robust H_∞ controller with the μ -synthesis controller in terms of the magnitude Bode plot of the transfer functions from r to e and from r to u , respectively. As shown in Figure 4.10, the robust H_∞ controller has better error rejection compared to the μ -synthesis controller (C1). More specifically, 0 dB crossing frequency is 21 Hz for robust H_∞ controller, while the one for μ -synthesis controller is 16 Hz. These values are compatible with bandwidth of the hand-shake disturbances (Figure B.2) and is much smaller than actuator bandwidth (which is about 150 Hz as shown in Figure 4.7).

4.3. Application to Large-scale OIS prototypes

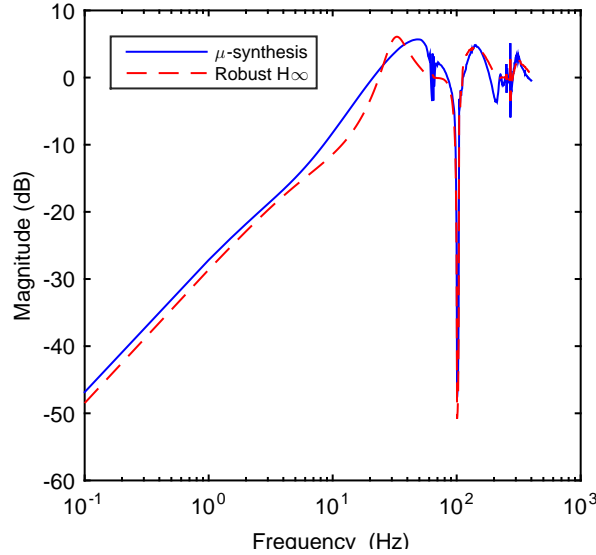


Figure 4.10: Frequency response of transfer function from reference to tracking error on nominal model

In Figure 4.11, the robust H_∞ controller uses less control effort compared to the μ -synthesis controller in low-frequency band (C2). The improvements achieved in tracking error and control effort can be associated with the ability of the proposed robust H_∞ controller design method to systematically generate decent initial guess for solution of the optimization problem corresponding to the proposed controller design problem as well as handling non-integer correction factors in the proposed uncertainty model. On the other hand, the iteration time for design of the robust H_∞ controller is slightly longer than that for the μ -synthesis controller because the μ -synthesis controller is designed using numerically-optimized off-the-shelf algorithms while custom-made algorithms are developed and used for design of the robust H_∞ controller.

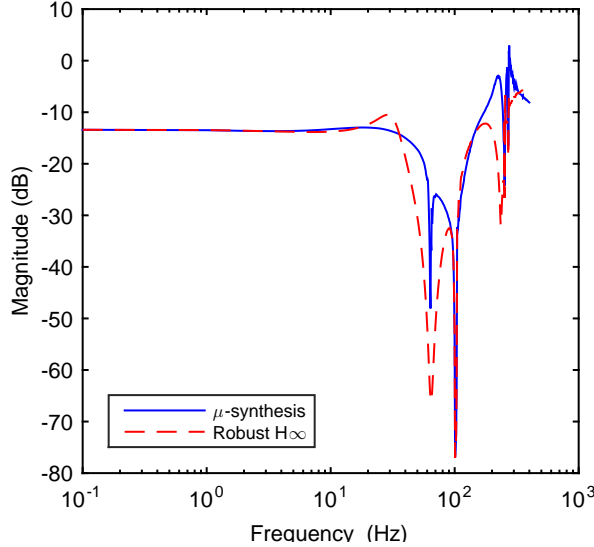


Figure 4.11: Frequency response of transfer function from reference to control input on nominal model

4.4 Application to Miniaturized OIS Prototypes

The application of the proposed method to large-scale in previous section, showed feasibility of the proposed method in an experimental setting and its capability to deal with physical product variabilities. This section extends the experimental study in the previous section to demonstrate the applicability of the proposed method to miniaturized OIS with mass-produced parts. Section 4.4.1 describe the miniaturized prototypes used in these experiments. In Section 4.4.2 the application of the proposed method to the miniaturized OIS prototypes are explained. Finally, experimental methodologies (introduced in Section 4.2) are used to obtain experimental results in Section 4.4.3.

4.4.1 Miniaturized OIS Prototypes

The details about miniaturized prototypes, including the mechanical design details, the product variabilities in miniaturized OISs, and the system identification results obtained by implementation of system identification tests used in the experiments of this section are explained in this subsection.

4.4. Application to Miniaturized OIS Prototypes

An example of a miniaturized OIS prototype is shown Figure 4.12. The size of the prototype is compatible with generic mobile phone dimensions. The lens platform is made of PlasWHITE photo-polymer and fabricated using a 3D printer in batch. The lens platform is installed on a base of same material by tolerance fitting. The coils and magnets are both commercial and mass-produced. The coils are held stationary by tolerance fitting to cylinders created in the base. The magnets are attached to the lens platform using a general-purpose glue. The numeric values for design parameters of the moving magnet actuators are tabulated in the third column of Table C.2 in Appendix C.

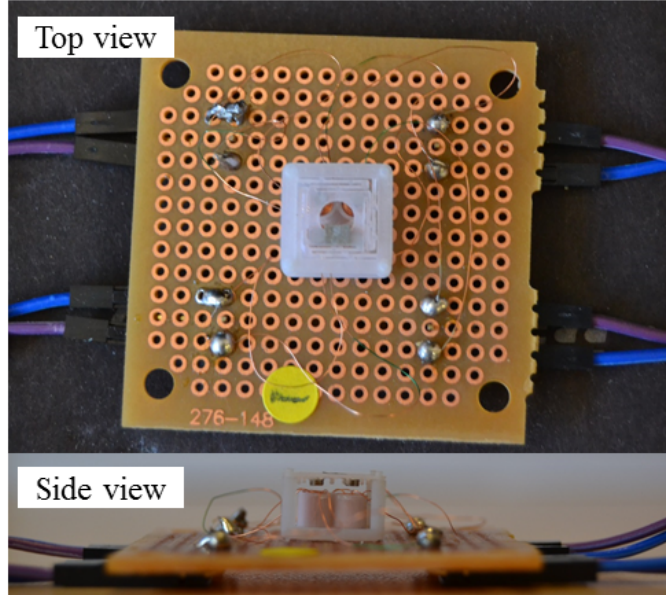


Figure 4.12: Miniaturized OIS prototype

Five miniaturized OIS prototypes are built as shown in Figure 4.13 to realize product variabilities. The OIS prototypes are named OIS 1–OIS 5. The sources contributing to product variabilities in miniaturized OIS prototypes are more complex compared to large-scale OISs. Even though no synthetic beam width variations are imposed in miniaturized OISs, there are numerous natural sources of variabilities in lens platform such as 3D printer’s fabrication tolerances, pillar residue, the curing post-processing that leads to clogging of the beams. Unlike large-scale OISs where different lens platforms shared a common base, separate bases are fabricated for each

4.4. Application to Miniaturized OIS Prototypes

lens platform in miniaturized OISs. The coils and magnets used in miniaturized OISs are off-the-shelf mass-produced coils and magnets with industry-quality product variabilities. The permanent magnets are attached using glue that adds significant variabilities specially in air-gap and coil-magnet misalignment compared to large-scale OISs where magnets are attached by magnetic force.

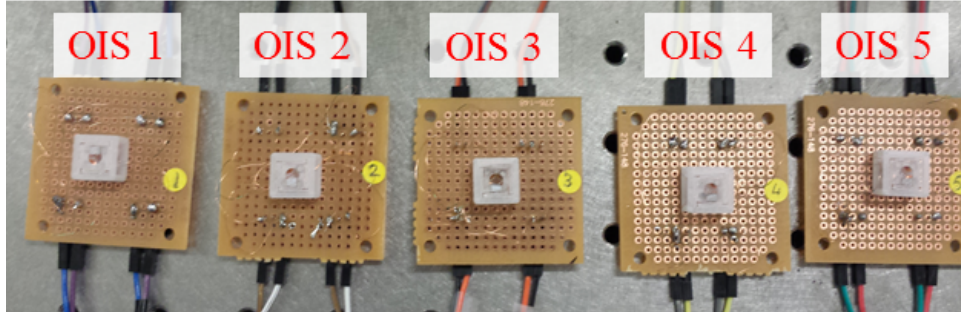


Figure 4.13: Product variabilities in miniaturized OISs

The dynamics of miniaturized OISs are characterized through system identification tests (described in Section 4.2.1) are performed on the miniaturized prototypes. Figure 4.14 shows the frequency responses of OIS 1–OIS 5. In general the structure of the frequency responses of miniaturized OISs are similar to simulation results (Figure 3.3) and large-scale results (Figure 4.7) because all share the same conceptual design. The bandwidth is about 300 Hz which is compatible with simulation results and sufficiently larger than the hand-shake disturbance bandwidth (20 Hz) shown in Figure B.2; however, since PlasWHITE has a relatively higher damping, the resonance modes have higher damping compared to stainless steel. In Figure 4.14, variations in natural frequencies and DC gain can be observed. In addition, the coupling of shifting mode appears in Figure 4.14 due to asymmetric actuation. The variations in frequency responses are larger and less correlated compared to simulation results (Figure 3.3) and large-scale results (Figure 4.7) due to added sources of product variabilities.

4.4.2 Robust Control of Miniaturized OIS Prototypes

The proposed method is applied to the miniaturized OIS prototypes based on the frequency-response database obtained in Figure 4.14. To apply the proposed method, first a dynamic uncertainty model is developed (introduced

4.4. Application to Miniaturized OIS Prototypes

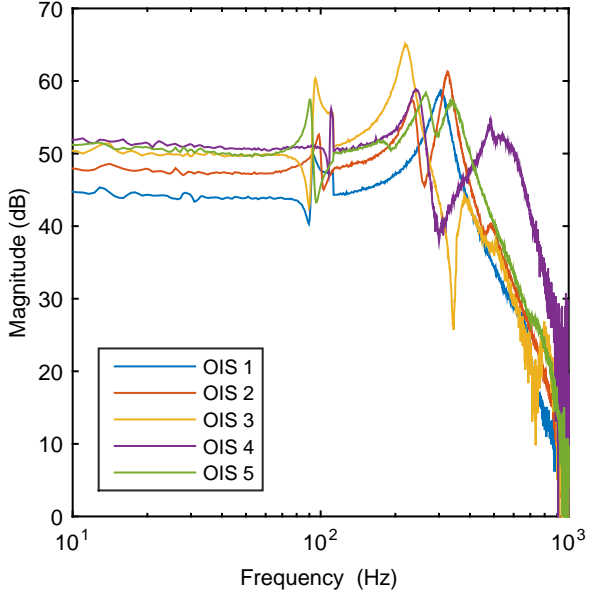


Figure 4.14: Frequency responses of miniaturized OISs

in Section 3.2), and then a robust H_∞ controller is designed (introduced in Section 3.3) for miniaturized OIS prototypes.

The data in Figure 4.14 suggests that in addition to uncertainties in natural frequencies and DC gains, the sharpness of resonance peaks corresponding to resonance modes 2, 3, and 4 also vary from one prototype to the other. To deal with this increased complexity in miniaturized OISs, a correlation is considered between the damping coefficients and the natural frequency of the second mode. To represent both increase and decrease of the damping ratio by a simple model, a linear correlation is defined as follows:

$$\xi_i = \underline{\xi}_i + \frac{\overline{\xi}_i - \underline{\xi}_i}{\overline{\omega}_{n_2} - \underline{\omega}_{n_2}} (\omega_{n_2} - \underline{\omega}_{n_2}), i = 1, \dots, 4. \quad (4.1)$$

The validity of linear assumption will be verified by comparing frequency responses of the model with the data. In addition to correlation of damping coefficient, the nominal values of the dynamics parameters and the correction factors are adjusted heuristically to achieve an appropriate model.

4.4. Application to Miniaturized OIS Prototypes

The parameters of the model (3.1) are obtained based on the system identification results. The numeric values of the model parameters are listed in the third column of the Table C.1. The multi-model uncertainty model obtained based on these parameter values are compared with the system identification results in Figure 4.15. The multi-model uncertainty model successfully captures the variations of frequency responses. A robust H_∞ controller is designed based on the multi-model uncertainty model. The controller design parameters (introduced in Figure 3.5 and Equation 3.10) for the robust H_∞ controller are listed in the third column of Table A.7.

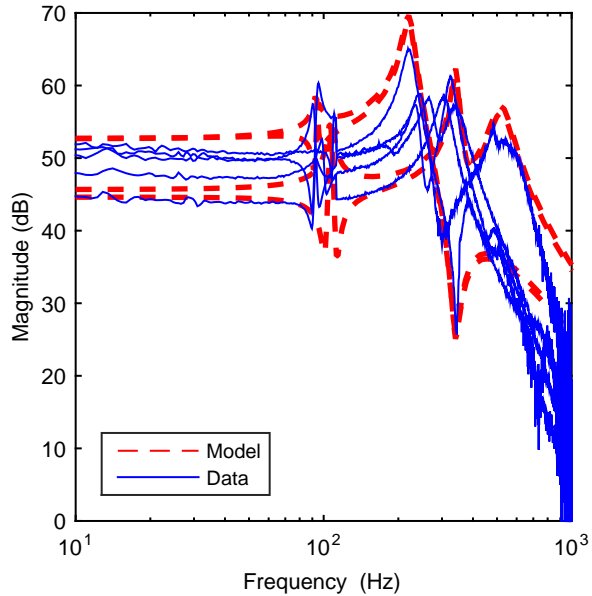


Figure 4.15: Multi-model dynamic uncertainty model of miniaturized OIS

4.4.3 Assessments of Robustness for Closed-loop Stability and Performance

Here, the experimental methodologies introduced in Section 4.2 are applied to the miniaturized OIS prototypes described in Section 4.4.1. The results of the robust closed-loop stability experiments are summarized in Table 4.3. In this experiment, the designed controllers in each row are implemented on different prototypes in each column. If the closed-loop system correspond-

4.4. Application to Miniaturized OIS Prototypes

ing to the controller and the prototype was stable, the cell at intersection of the row associated with the controller and the column associated with the prototype is designated by a check mark (\checkmark), otherwise it is designated by a cross mark (\times) is used to show that the closed-loop system was unstable. According to Table 4.3, None of nominal controllers can stabilize the closed-loop system corresponding to all OISs because the nominal controller design methods do not take uncertainties into account. On the other hand, both robust controllers (robust H_∞ controller and μ -synthesis controller) stabilized the closed-loop system for all prototypes (C3) because the robust controller design methods take uncertainties into account and guarantees robust closed-loop stability against uncertainties in the design stage.

Table 4.3: Assessment of closed-loop stability robustness in miniaturized OISs

	OIS 1	OIS 2	OIS 3	OIS 4	OIS 5
PID	\times	\checkmark	\checkmark	\times	\times
lead-lag	\checkmark	\checkmark	\checkmark	\times	\times
LQG	\times	\times	\checkmark	\times	\times
H_∞	\times	\times	\checkmark	\times	\times
μ -synthesis	\checkmark	\checkmark	\checkmark	\checkmark	\checkmark
Robust H_∞	\checkmark	\checkmark	\checkmark	\checkmark	\checkmark

The results of time-domain performance testes are shown in Figure 4.16 in form of bar diagrams. In the bar diagrams, the solid bars indicates the mean values of the RMS error while the upper limit of error bars denote the worst-case RMS error. The results are consistent with simulation results (Figure 3.9) and large-scale experimental results (Figure 4.9). The robust controllers reduce the mean values (C1) and degradation (C3) of tracking error compared to nominal controllers because the robust controller design methods take uncertainties into account and systematically optimize robust closed-loop performance against uncertainties to minimize conservatism. This improvement is shown against variations in hand-shake signals, OIS uncertainties, and both. The improvements achieved in miniaturized OIS are less than simulation results (Figure 3.9) and large-scale experimental results (Figure 4.9) because the uncertainties that has to be considered by the robust controller design methods are larger and more complex. Therefore, relatively modest performance is achievable. More specifically, analysis shows that hand-shake disturbances could be suppressed more than 31%

4.4. Application to Miniaturized OIS Prototypes

better than nominal controllers.

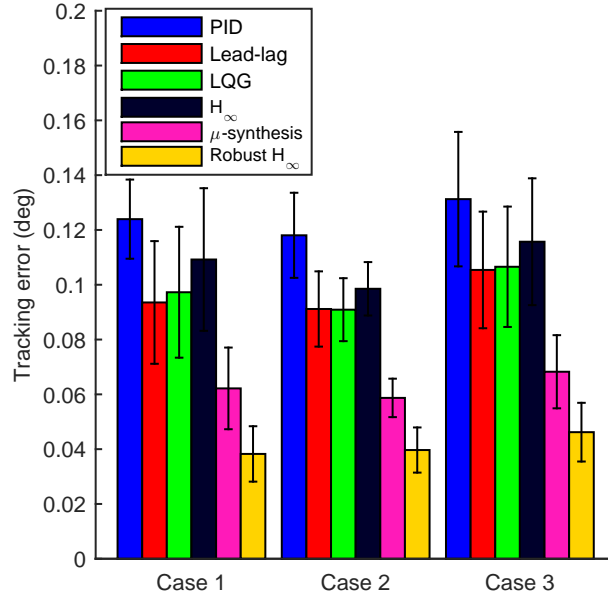


Figure 4.16: Time-domain performance assessment of different controllers on miniaturized OISs

The robust H_{∞} controller is compared with the μ -synthesis controller in Table 4.4. The order of robust H_{∞} controller is much smaller than that of μ -synthesis controller (C4) because it mathematically constraints the controller order. The improvements in order is far more significant than the large-scale case because as uncertainties become larger and more complex (compare Figure 4.14 with Figure 4.7), order of μ -synthesis controller drastically increases. In Table 4.4, the values outside parenthesis for tracking error and control effort are mean values, while the ones inside parenthesis are the worst-case degradations. The robust H_{∞} controller reduces the mean (C1) and degradation (C3) of the tracking error as well as mean (C2) and the degradation (C3) of the control effort compared to the μ -synthesis controller. The improvements achieved are smaller compared to ones in simulations. This can be associated with the increased variabilities in miniaturized OISs compared to large-scale OISs (compare Figure 4.14 with Figure 4.7) because as uncertainties become larger and more complex, conservativeness of robust controllers increases.

4.4. Application to Miniaturized OIS Prototypes

Table 4.4: Summary comparison of μ -synthesis with Robust H_∞ on miniaturized OISs

	μ -synthesis	Robust H_∞
Designed order (-)	289	11
Reduced order (-)	61	10
Tracking error (deg)	0.0470 (0.0105)	0.0376 (0.0095)
Control effort (mAh)	0.9157 (0.3395)	0.8940 (0.3337)
Computation time (s)	2443	303

Figure 4.17 and Figure 4.18 show the results of the frequency-domain performance tests. Figure 4.17 and Figure 4.18 compares the robust H_∞ controller with the μ -synthesis controller in terms of the magnitude Bode plot of the transfer functions from r to e and from r to u , respectively. As shown in Figure 4.17, the robust H_∞ controller has better error rejection compared to the μ -synthesis controller (C1). More specifically, 0 dB crossing frequency is 24 Hz for robust H_∞ controller, while the one for μ -synthesis controller is 20 Hz. These values are compatible with bandwidth of the hand-shake disturbances (Figure B.2) and is much smaller than actuator bandwidth (which is about 150 Hz as shown in Figure 4.14).

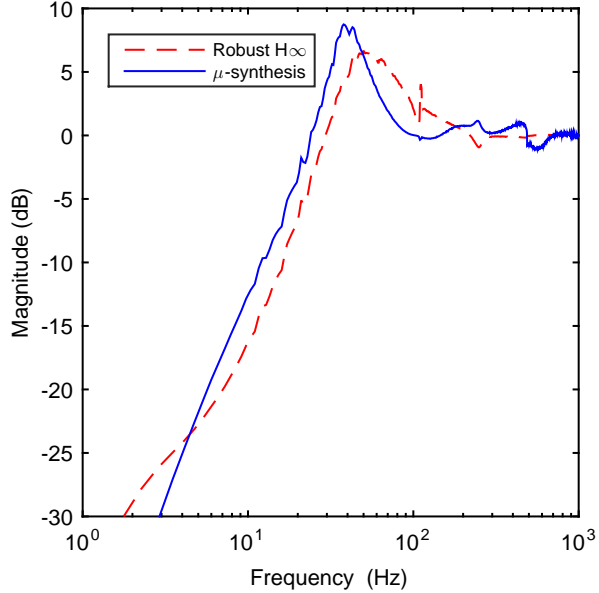


Figure 4.17: Frequency response of transfer function from reference to tracking error on nominal model

In Figure 4.18, the robust H_∞ controller uses less control effort compared to the μ -synthesis controller in low-frequency band (C2). The improvements achieved in tracking error and control effort can be associated with the ability of the proposed robust H_∞ controller design method to systematically generate a good initial guess for the solution of the optimization problem corresponding to the proposed controller design problem as well as handling non-integer correction factors in the proposed uncertainty model. On the other hand, the iteration time for design of the robust H_∞ controller is slightly higher than the μ -synthesis controller because the μ -synthesis controller is designed using numerically-optimized off-the-shelf algorithms while custom-made algorithms are developed and used for design of the robust H_∞ controller.

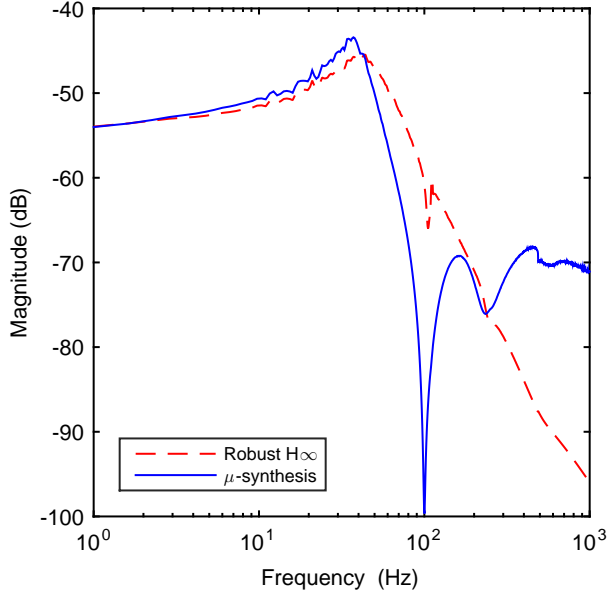


Figure 4.18: Frequency response of transfer function from reference to control input on nominal model

Table 4.5 compares the percent improvements achieved in tracking performance by the robust H_∞ controller with conventional controllers in three case studies. The conventional controllers are the nominal controllers and the μ -synthesis controller. The nominal controllers are represented by the mean value of the four (PID, lead-lag, LQG, and H_∞ controller) controllers. The percent improvements are calculated by normalization of the tracking error signal RMS values with the RMS value of the mean RMS value of the hand-shake disturbance signals (Figure B.1). In each cell, the value on top corresponds to the improvement in nominal tracking performance (solid bars in Figure 3.9, 4.9, 4.16) while the value at bottom shows the improvement in degradation of the tracking performance error bars in Figure 3.9, 4.9, 4.16.

In comparison with the nominal controllers, the improvements in miniaturized is less than large-scale and improvements in large-scale is less than simulations because the uncertainties that has to be considered by the robust controller design methods are larger and more complex. Therefore, relatively modest performance is achievable. On the other hand, compared to the μ -synthesis controller the improvements in miniaturized is more than

4.5. Practical Implications of the Experimental Result

Table 4.5: Percent improvements achieved by robust H_∞ controller compared to conventional controllers for different case studies

	Simulations	Large-scale	Miniaturized
Nominal controllers	43.8108	40.8558	30.8558
	7.8328	6.9234	5.4054
μ-synthesis controller	2.9909	3.0315	9.9324
	0.8108	0.1238	1.1936

large-scale and improvements in large-scale is more than simulations. This can be associated with the increased variabilities in miniaturized OISs compared to large-scale OISs (compare Figure 4.14 with Figure 4.7) because as uncertainties become larger and more complex, conservativeness of the μ -synthesis controller controllers increases.

4.5 Practical Implications of the Experimental Result

Through experimental work presented in Section 4.3 and Section 4.4, it is demonstrated that the proposed method is implementable in an experimental setting and provides closed-loop stability and performance advantages when used on miniaturized OISs. On top of this, the proposed method offers practically economic, systematic, and universal approach to controller design for the OISs.

Using the proposed method in practice, a single controller can be designed and implemented on the entire product set. This can save manufacturers time and cost to test, model, and design controllers for individual OISs. Specifically, all controller design methods include trial-and-error that makes controller design for individual OISs even more overwhelming.

The proposed method offers practical advantages also over other robust controllers. First of all, it provides a systematic method of optimizing the closed-loop performance. This advantage saves a lot of trial-and-error efforts that has to go into de-tuning of nominal controllers to recover robust closed-loop stability/performance for the uncertainty region in Section 4.2.2. Secondly, as demonstrated in Section 4.4.3 increase in uncertainties leads to drastic increase in iteration time and controller order of the μ -synthesis controller. This makes the μ -synthesis controller design extremely tedious because on top of the long iteration time, a tedious sequential procedure

4.5. Practical Implications of the Experimental Result

encompassing order reduction and closed-loop stability/performance analysis for the uncertainty region is needed to design the controller. Finally, the proposed method can design a robust controller for the entire production line based on only a limited number of representative samples, thus decreasing system identification efforts significantly.

Furthermore, the proposed method takes universality into account. The proposed method does not make any assumptions about any specific parameter value/range. Therefore, the proposed method can be directly applied to any detailed designs (e.g. material, dimensions, component parameters, etc.) of OIS as long as it complies with the same conceptual design reviewed in Section 2.1. The detailed design of OIS could vary rapidly to adapt this conceptual design to different mobile phones or different models of the same mobile phone according to cost, size, performance, and power requirements.

Finally, low-cost manufacturing techniques can be employed for fabrication of the lens-platform and assembly of moving-magnet actuators without concern about their tolerances. Therefore, final price can be reduced which is an important factor in mobile phone market.

The practical advantages of the proposed method can be exploited to reduce final cost of the OISs to replace software-based algorithms. Replacing OISs with software-based algorithms can improve the image quality of the mobile phone cameras.

Chapter 5

Conclusions

In conclusion, the proposed robust controller design method was shown to be a systematic scheme to design a controller that can deal with product variabilities in minaturized OISs and is simple enough to be implementable in a mobile phone device. The experimental results demonstrates feasibility of the proposed method in an experimental setting, and its capability to deal with physical product variabilities. This can expand application of miniaturized and low-cost OISs to replace conventional post-processing algorithms currently implemented on many mobile phone devices, which is a big step to improve image quality of the mobile phone cameras.

In this chapter, we summarize important results that supports the drawn conclusions, list contributions of this thesis, and point out some potential future work.

5.1 Summary

In this thesis, a robust controller design method was developed for a novel magnetically-actuated lens-tilting OIS designed for mobile phone devices to overcome challenges arising from product variabilities of micro-manufacturing processes and implementation limitations of the controller on mobile phone devices.

The details of the OIS including its mechanical design (Section 2.1), control system configuration (Section 2.2), and performance objectives and specifications (Section 2.3) were reviewed in Chapter 2. In Chapter 3, first a comprehensive FEA was performed on the model of the reviewed OIS to analyze the effect of beam width variations and force imbalances on tilting dynamics (Section 3.1). Using combination of FEA results with knowledge of mechanical design of OIS, a model structure and an uncertainty structure were proposed for tilting dynamics in Section 3.2. To deal with the model, a robust controller design method was proposed in Section 3.1 that considers uncertainties through vertices of the uncertainty region to design a low-order controller. The proposed method transformed the controller design problem to an optimization problem that could be solved employing

5.1. Summary

efficient and reliable algorithms. In the optimization problem, constraint functions represented robust closed-loop stability criterion and the objective function represented worst-case closed-loop performance. Therefore, closed-loop stability could be guaranteed against uncertainties while optimizing the worst-case performance. To solve the optimization problem, the proposed method provided a systematic way of obtaining a decent initially-feasible solution to avoid conservatism.

Chapter 4 presented the experimental results and discussions. Section 4.1 described the experimental setups used for system identification (Section 4.1.1) and closed-loop implementation in time-domain (Section 4.1.2) and frequency-domain (Section 4.1.3). Then, some experimental methodologies were used based on the setups for performing the tests and analysing the results, including system identification (Section 4.2.1), closed-loop stability (Section 4.2.2), and closed-loop implementation in time-domain (Section 4.2.3) and frequency-domain (Section 4.2.4). Then, same setups and methodologies were used to implement the proposed method on large-scale (Section 4.3) and miniaturized (Section 4.4) OISs.

In Section 4.3, experimental results obtained from the application of the proposed method on large-scale OISs were presented. This experiment had two objectives: (1) deal with physical product variabilities (2) implement the proposed method in an experimental setting. The large-scale prototypes were scaled 5 times the original conceptual design. The physical product variabilities in miniaturized OISs were mimicked by intentional beam width variations in large-scale lens-platforms. Moreover, the moving-magnet actuators and the base were custom-made and used commonly across all lens-platforms. The proposed method was directly applied to large-scale OISs by experimental identification of dynamics parameters and uncertainty parameters. Through large-scale experiments, it was shown that the proposed method is executable in an experimental setting and capable of dealing with physical product variabilities. The experimental results suggested that robust controllers designed based on the proposed method could achieve closed-loop stability for all OISs while nominal controllers cannot. Moreover, the robust controllers reduced the tracking error to almost half compared to de-tuned versions of the nominal controllers in general. The propose robust H_∞ method also outperformed conventional robust controller design methods, namely μ -synthesis. The proposed robust H_∞ method reduced the nominal tracking error by about 3% and its variabilities by about 0.1% with almost the same control effort. The controller order was decreased to half while the iteration time was increased slightly compared to μ -synthesis.

Section 4.4 explained experimental results obtained from the application

5.1. Summary

of the proposed method to miniaturized OISs to demonstrate applicability of the method to miniaturized OISs containing mass-produced parts. The dimensions of the miniaturized prototypes were compatible with mobile phones, and their parts were fabricated in a batch-based manner with no intentional uncertainties. System identification results showed increase in magnitude and complexity of the product variabilities compared to simulation and large-scale results; however, the proposed method was shown to be applicable to miniaturized OISs through some mild modifications. The experimental results suggested that robust controllers designed based on the proposed method could achieve closed-loop stability for all OISs while conventional nominal controllers cannot. Moreover, the robust controllers reduced the tracking error to almost half compared to de-tuned versions of the conventional nominal controllers in general. The complexity of the uncertainties in miniaturized OISs made μ -synthesis controller design method practically challenging considering controller order and iteration time. The proposed robust H_∞ method outperformed μ -synthesis in terms of controller order, iteration time, and closed-loop performance due to increased uncertainties. The proposed robust H_∞ method reduced the nominal tracking error by about 10% and its variabilities by about 1.2% while also reducing control effort by 2.4% and its variabilities by 1.7%. The controller order is reduced 6 folds, and iteration times 8 folds.

In comparison with the conventional nominal controllers, the improvements in miniaturized OISs is less than large-scale OISs, and improvements in large-scale is less than simulations because the uncertainties that has to be considered by the robust controller design methods are larger and more complex. Therefore, relatively modest performance is achievable. On the other hand, compared to the μ -synthesis controller the improvements in miniaturized is more than large-scale and improvements in large-scale is more than simulations. This can be associated with the increased variabilities in miniaturized OISs compared to large-scale OISs because as uncertainties become larger and more complex, conservativeness of the μ -synthesis controller controllers increases.

The improvements achieved in the control of the magnetically-actuated lens-tilting optical image stabilizer can expand its application in mobile phone cameras to replace post-processing algorithms which is a significant step towards superior image qualities in mobile phone cameras.

5.2. Contributions

5.2 Contributions

The main contributions of this thesis can be outlined as follows:

- FEA was performed on CAD model of the miniaturized magnetically-actuated lens-tilting OISs to characterize their dynamics and uncertainties.
- A dynamic uncertainty model is developed based on FEA results and mechanical design of miniaturized magnetically-actuated lens-tilting OISs to describe dynamics and uncertainties of controller design purposes.
- A robust controller design problem is formulated to deal with the developed dynamic uncertainty model of OIS
- Executability of the proposed modeling and controller design method is demonstrated in an experimental setting with physical product variabilities.
- Applicability of the proposed modeling and controller design method to real miniaturized OIS production lines were demonstrated by implementation miniaturized OISs.
- Design guidelines are developed for the conventional nominal controllers (i.e, PID, lead-lag, LQG, and H_∞ controller) tailored for the magnetically-actuated lens-tilting OIS application (Appendix A).

5.3 Future Work

The magnetically-actuated lens-tilting OIS is a novel conceptual design indicating great potential for OIS in mobile phone applications as discussed in Section 1.3.2. This novel concept can benefit greatly from further research and development on mechanical design, modeling, and controller design. In future, the research presented in this thesis can be further expanded as summarized next.

5.3.1 Multiple Robust H_∞ Control

The proposed method treats the uncertainty region (Figure 3.4) in a monolithic way; however, this approach leads to conservatism when uncertainties

5.3. Future Work

are large and complex as shown in small-scale experiments. To reduce conservatism, the multiple robust H_∞ control theories [2, 62] divide the uncertainty region into several subregions and design a robust controller for each subregion.

5.3.2 Fixed-order Robust H_∞ Control

Another limitation of the proposed method is that the controller order is correlated with order of the plant model. Therefore, the closed-loop performance is compromised if less controller order is desired. To improve this trade-off, fixed-order robust H_∞ control theories [48, 49] explicitly incorporate controller order constraint in the mathematical formulation of the robust controller design problem. Therefore, an arbitrarily simple controller can be designed based on an arbitrarily complex plant model to optimize closed-loop performance; however, it is not trivial whether fixed-order robust H_∞ control theories can offer advantages compared to the proposed method for this application because in general they typically include some conservatism to incorporate the controller order constraint in the mathematical formulation.

5.3.3 Implementation on Physical Mobile Phone Cameras

Finally, the experimental results obtained in this thesis represent the image blur by the RMS value of the tracking error signal that might not be realistic enough. To perform a more realistic assessment, the OIS should be integrated with a physical mobile phone devices where optical metrics of image blur (e.g stabilization rate and sharpness rate [43]) can be measured out of the taken images.

Bibliography

- [1] K. J. Åström, “Limitations on control system performance,” *European Journal of Control*, vol. 6, no. 1, pp. 2–20, 2000.
- [2] E. Azadi Yazdi, *Multiple Robust Controllers Design for Linear Uncertain Systems*. University of British Columbia, 2011.
- [3] G. Balas, R. Chiang, A. Packard, and M. Safonov, “Robust control toolbox,” *For Use with Matlab. Users Guide, Version*, vol. 3, 2005.
- [4] M. Boudaoud, Y. Haddab, and Y. Le Gorrec, “Modeling and optimal force control of a nonlinear electrostatic microgripper,” *IEEE/ASME Transactions on Mechatronics*, vol. 18, no. 3, pp. 1130–1139, 2013.
- [5] S. Boyd and L. Vandenberghe, *Convex Optimization*. Cambridge University Press, 2004.
- [6] S. P. Boyd, L. El Ghaoui, E. Feron, and V. Balakrishnan, *Linear Matrix Inequalities in System and Control Theory*. SIAM, 1994, vol. 15.
- [7] R. Bracewell, *The Fourier Transform and Its Applications*. McGraw-Hill, 1965, vol. 5.
- [8] B. Cardani, “Optical image stabilization for digital cameras,” *Control Systems Magazine, IEEE*, vol. 26, no. 2, pp. 21–22, 2006.
- [9] H. J. Chang, P. J. Kim, D. S. Song, and J. Y. Choi, “Optical image stabilizing system using multirate fuzzy PID controller for mobile device camera,” *IEEE Transactions on Consumer Electronics*, vol. 55, no. 2, pp. 303–311, 2009.
- [10] J.-C. Chiou, C.-C. Hung, and C.-Y. Lin, “Design, fabrication and actuation of a MEMS-based image stabilizer for photographic cell phone applications,” *Journal of Micromechanics and Microengineering*, vol. 20, no. 7, pp. 1–11, 2010.

Bibliography

- [11] C.-W. Chiu, P. C.-P. Chao, N. Y.-Y. Kao, and F.-K. Young, “Optimal design and experimental verification of a magnetically actuated optical image stabilization system for cameras in mobile phones,” *Journal of applied physics*, vol. 103, no. 7, pp. 07F136–1–07F136–3, 2008.
- [12] A. Chowdhury, R. Darveaux, J. Tome, R. Schoonejongan, M. Reifel, A. De Guzman, S. S. Park, Y. W. Kim, and H. W. Kim, “Challenges of megapixel camera module assembly and test,” in *Electronic Components and Technology Conference, 2005. Proceedings. 55th. IEEE*, 2005, pp. 1390–1401.
- [13] R. de Callafon, R. Nagamune, and R. Horowitz, “Robust dynamic modeling and control of dual-stage actuators,” *IEEE Transactions on Magnetics*, vol. 42, no. 2, pp. 247–254, 2006.
- [14] J. Ding, M. Tomizuka, and H. Numasato, “Design and robustness analysis of dual stage servo system,” in *Proceedings of the American Control Conference, 2000*, pp. 2605–2609.
- [15] J. Fei and C. Batur, “A novel adaptive sliding mode controller for MEMS gyroscope,” in *Proceedings of the 46th IEEE Conference on Decision and Control, 2007*, pp. 3573–3578.
- [16] J. Fei and J. Zhou, “Robust adaptive control of MEMS triaxial gyroscope using fuzzy compensator,” *IEEE Transactions on Systems, Man, and Cybernetics, Part B: Cybernetics*, vol. 42, no. 6, pp. 1599–1607, 2012.
- [17] P. Gahinet, A. Nemirovskii, A. J. Laub, and M. Chilali, “The lmi control toolbox,” in *Proceedings of the IEEE conference on decision and control, 1994*, pp. 2038–2038.
- [18] B. Golik, G. Fischer, and D. I. D. Wueller, “Development of a test method for image stabilizing systems,” Ph.D. dissertation, Diploma Thesis at the Department of Imaging Sciences and Media Technology Cologne University of Applied Sciences, 2006.
- [19] Q. Hao, X. Cheng, J. Kang, and Y. Jiang, “An image stabilization optical system using deformable freeform mirrors,” *Sensors*, vol. 15, no. 1, pp. 1736–1749, 2015.
- [20] H. G. Harno and R. S. K. Woon, “Robust H_∞ stabilization of a hard disk drive system with a single-stage actuator,” in *Proceedings of the*

Bibliography

- IOP Conference Series: Materials Science and Engineering, 2015*, pp. 969–975.
- [21] M. Hecke and W. Schomburg, “Review on micro molding of thermoplastic polymers,” *Journal of Micromechanics and Microengineering*, vol. 14, no. 3, pp. R1–R14, 2004.
 - [22] D. Hernandez, S.-S. Park, R. Horowitz, and A. K. Packard, “Dual-stage track-following servo design for hard disk drives,” in *Proceedings of the American Control Conference, 1999*, pp. 4116–4121.
 - [23] G. Herrmann and G. Guo, “HDD dual-stage servo-controller design using a μ -analysis tool,” *Control Engineering Practice*, vol. 12, no. 3, pp. 241–251, 2004.
 - [24] X. Huang, R. Horowitz, and Y. Li, “Design and analysis of robust track-following controllers for dual-stage servo systems with an instrumented suspension,” in *Proceedings of the American Control Conference, 2005*, pp. 1126–1131.
 - [25] X. Huang, R. Nagamune, and R. Horowitz, “A comparison of multirate robust track-following control synthesis techniques for dual-stage and multisensing servo systems in hard disk drives,” *IEEE Transactions on Magnetics*, vol. 42, no. 7, pp. 1896–1904, 2006.
 - [26] A. Izadbakhsh and S. Rafiei, “Robust control methodologies for optical micro electro mechanical system-new approaches and comparison,” in *Proceedings of the Power Electronics and Motion Control Conference, 2008*, pp. 2102–2107.
 - [27] S. Kanev, C. Scherer, M. Verhaegen, and B. de Schutter, “Robust output-feedback controller design via local BMI optimization,” *Automatica*, vol. 40, no. 7, pp. 1115–1127, 2004.
 - [28] P. Kauhanen and J. Rouvinen, “Actuator for miniature optical image stabilizer,” in *Proceedings of the 10th International Conference on New Actuators, 2006*, pp. 549–552.
 - [29] M. Komori and T. Hirakawa, “A magnetically driven linear microactuator with new driving method,” *IEEE/ASME Transactions on Mechatronics*, vol. 10, no. 3, pp. 335–338, 2005.

Bibliography

- [30] C. Lee and S. M. Salapaka, “Fast robust nanopositioning: A linear-matrix-inequalities-based optimal control approach,” *IEEE/ASME Transactions on Mechatronics*, vol. 14, no. 4, pp. 414–422, 2009.
- [31] S.-K. Lee and J.-H. Kong, “An implementation of closed-loop optical image stabilization system for mobile camera,” in *Proceedings of the IEEE International Conference on Consumer Electronics (ICCE)*, 2014, pp. 45–46.
- [32] S.-K. Lee, I.-H. Kook, and J.-H. Kong, “A study of mobile optical image stabilization system for mobile camera,” in *Proceedings of the International SoC Design Conference (ISOCC)*, 2012, pp. 212–214.
- [33] T.-H. S. Li and C.-C. Chen, “Extended Kalman filter based hand-shake detector for optical image stabilization using a low cost gyroscope,” *IEEE Transactions on Consumer Electronics*, vol. 59, no. 1, pp. 113–121, 2013.
- [34] T.-H. S. Li, C.-C. Chen, and Y.-T. Su, “Optical image stabilizing system using fuzzy sliding-mode controller for digital cameras,” *IEEE Transactions on Consumer Electronics*, vol. 58, no. 2, pp. 237–245, 2012.
- [35] W. Li and P. X. Liu, “Robust adaptive tracking control of uncertain electrostatic micro-actuators with H_∞ performance,” *Mechatronics*, vol. 19, no. 5, pp. 591–597, 2009.
- [36] ———, “Adaptive tracking control of an MEMS gyroscope with H_∞ performance,” *Journal of Control Theory and Applications*, vol. 9, no. 2, pp. 237–243, 2011.
- [37] Y. Li and R. Horowitz, “Mechatronics of electrostatic microactuators for computer disk drive dual-stage servo systems,” *IEEE/ASME Transactions on Mechatronics*, vol. 6, no. 2, pp. 111–121, 2001.
- [38] C.-Y. Lin and J.-C. Chiou, “Design, fabrication and actuation of four-axis thermal actuating image stabiliser,” *IET Micro & Nano Letters*, vol. 6, no. 7, pp. 549–552, 2011.
- [39] M. Malisoff, F. Mazenc, and M. de Queiroz, “Tracking and robustness analysis for controlled microelectromechanical relays,” *International Journal of Robust and Nonlinear Control*, vol. 18, no. 18, pp. 1637–1656, 2008.

Bibliography

- [40] D. Meeker, “Finite element method magnetics,” version 4.2 (25Oct2015 Build), <http://www.femm.info>.
- [41] S. Mittal and C.-H. Menq, “Precision motion control of a magnetic suspension actuator using a robust nonlinear compensation scheme,” *Mechatronics, IEEE/ASME Transactions on*, vol. 2, no. 4, pp. 268–280, 1997.
- [42] R. Nagamune, X. Huang, and R. Horowitz, “Robust control synthesis techniques for multirate and multisensing track-following servo systems in hard disk drives,” *Journal of Dynamic Systems, Measurement, and Control*, vol. 132, no. 2, pp. 021 005–1–021 005–10, 2010.
- [43] B. Nielsen, “Resolution, unsharpness and mtf,” 1980.
- [44] Y. Okamoto and R. Yoshida, “Development of linear actuators using piezoelectric elements,” *Electronics and Communications in Japan (Part III: Fundamental Electronic Science)*, vol. 81, no. 11, pp. 11–17, 1998.
- [45] R. Palm, “Robust control by fuzzy sliding mode,” *Automatica*, vol. 30, no. 9, pp. 1429–1437, 1994.
- [46] P. Pournazari, R. Nagamune, and M. Chiao, “A concept of a magnetically-actuated optical image stabilizer for mobile applications,” *IEEE Transactions on Consumer Electronics*, vol. 60, no. 1, pp. 10–17, 2014.
- [47] P. Rawat and J. Singhai, “Review of motion estimation and video stabilization techniques for hand held mobile video,” *Signal & Image Processing: An International Journal (SIPIJ) Vol*, vol. 2, 2011.
- [48] M. S. Sadabadi and A. Karimi, “Fixed-order H_∞ and H_2 controller design for continuous-time polytopic systems: An lmi-based approach,” in *Control Conference (ECC), 2013 European*. Ieee, 2013, pp. 1132–1137.
- [49] ——, “An LMI formulation of fixed-order H_∞ and H_2 controller design for discrete-time systems with polytopic uncertainty,” in *Decision and Control (CDC), 2013 IEEE 52nd Annual Conference on*. IEEE, 2013, pp. 2453–2458.
- [50] H. S. Sane, “Energy-based control for MEMS with one-sided actuation,” in *American Control Conference, 2006*. IEEE, 2006, pp. 6–12.

Bibliography

- [51] E. H. Sarraf, M. Sharma, and E. Cretu, “Novel sliding mode control for MEMS-based resonators,” *Procedia Engineering*, vol. 25, pp. 1305–1308, 2011.
- [52] ——, “Novel band-pass sliding mode control for driving MEMS-based resonators,” *Sensors and Actuators A: Physical*, vol. 186, pp. 154–162, 2012.
- [53] M. Shavezipur, K. Ponnambalam, A. Khajepour, and S. Hashemi, “Fabrication uncertainties and yield optimization in MEMS tunable capacitors,” *Sensors and Actuators A: Physical*, vol. 147, no. 2, pp. 613–622, 2008.
- [54] E. Simon, B. Berge, F. Fillit, H. Gaton, M. Guillet, O. Jacques-Sermet, F. Laune, J. Legrand, M. Maillard, and N. Tallaron, “Optical design rules of a camera module with a liquid lens and principle of command for af and ois functions,” in *Photonics Asia 2010*. International Society for Optics and Photonics, 2010, pp. 784903–784903.
- [55] C. P. B. Siu, H. Zeng, and M. Chiao, “Magnetically actuated mems microlens scanner for in vivo medical imaging,” *Optics express*, vol. 15, no. 18, pp. 11 154–11 166, 2007.
- [56] C. Siu, H. Wang, H. Zeng, and M. Chiao, “Dual-axes confocal microlens for raman spectroscopy,” in *Micro Electro Mechanical Systems, 2009. MEMS 2009. IEEE 22nd International Conference on*. IEEE, 2009, pp. 999–1002.
- [57] M.-G. Song, H.-W. Baek, N.-C. Park, K.-S. Park, T. Yoon, Y.-P. Park, and S.-C. Lim, “Development of small sized actuator with compliant mechanism for optical image stabilization,” *IEEE Transactions on Magnetics*, vol. 46, no. 6, pp. 2369–2372, 2010.
- [58] M.-G. Song, Y.-J. Hur, N.-C. Park, Y.-P. Park, K.-S. Park, S.-C. Lim, and J.-H. Park, “Development of small sized actuator for optical image stabilization,” in *Proceedings of the International Symposium on Optomechatronic Technologies, 2009*, pp. 152–157.
- [59] Y. Sun, C. R. Fowkes, N. Gindy, and R. K. Leach, “Variation risk analysis: MEMS fabrication tolerance for a micro CMM probe,” *The International Journal of Advanced Manufacturing Technology*, vol. 47, no. 9-12, pp. 1113–1120, 2010.

Bibliography

- [60] S. G. Tzafestas and G. G. Rigatos, “A simple robust sliding-mode fuzzy-logic controller of the diagonal type,” *Journal of Intelligent and Robotic Systems*, vol. 26, no. 3-4, pp. 353–388, 1999.
- [61] F. Xiao, J. E. Farrell, P. B. Catrysse, and B. Wandell, “Mobile imaging: the big challenge of the small pixel,” in *IS&T/SPIE Electronic Imaging*. International Society for Optics and Photonics, 2009, pp. 72500K–72506K.
- [62] E. A. Yazdi and R. Nagamune, “Multiple robust h controller design using the nonsmooth optimization method,” *International Journal of Robust and Nonlinear Control*, vol. 20, no. 11, pp. 1197–1212, 2010.
- [63] D. Yeom, “Optical image stabilizer for digital photographing apparatus,” *IEEE Transactions on Consumer Electronics*, vol. 3, no. 55, pp. 1028–1031, 2009.
- [64] D. Yeom, N. Park, and S. Jung, “Digital controller of novel voice coil motor actuator for optical image stabilizer,” in *Proceedings of the International Conference on Control, Automation and Systems, 2007*, pp. 2201–2206.
- [65] H.-C. Yu and T. Liu, “Adaptive model-following control for slim voice coil motor type optical image stabilization actuator,” *Journal of Applied Physics*, vol. 103, no. 7, pp. 07F114–1–07F114–3, 2008.
- [66] ——, “Sliding mode control using virtual eigenvalue method for compact optical image stabilization actuators,” *IEEE Transactions on Magnetics*, vol. 44, no. 11, pp. 4074–4077, 2008.
- [67] K. Yuan, *A 3D Printing and Moulding Method of the Fabrication of a Miniature Voice Coil Motor Actuator*, 2015, university of British Columbia.
- [68] X. Zhang, B. Koo, S. M. Salapaka, J. Dong, and P. M. Ferreira, “Robust control of a mems probing device,” *IEEE/ASME Transactions on Mechatronics*, vol. 19, no. 1, pp. 100–108, 2014.
- [69] P. Zhao, A. Alizadegan, R. Nagamune, and M. Chiao, “Robust control of large-scale prototypes for miniaturized optical image stabilizers with product variations,” in *Proceedings of the 54th Annual Conference of the Society of Instrument and Control Engineers of Japan (SICE), 2015*, pp. 734–739.

- [70] K. Zhou, J. C. Doyle, and K. Glover, *Robust and Optimal Control*. Prentice Hall, New Jersey, 1996.
- [71] G. Zhu, J. Penet, and L. Saydy, “Robust control of an electrostatically actuated MEMS in the presence of parasitics and parametric uncertainties,” in *Proceedings of the American Control Conference, 2006*, pp. 1233–1238.

Appendix A

Controller Design Methodologies and Parameter Values

This section presents methodologies used for designing baseline controllers and resulting parameter values for lens-tilting OIS.

A.1 Notch Filter Design

Notch filter is used in series with classical controllers, namely PID and lead-lag, to deal with lightly-damped modes of OIS. The notch filter is parametrized as:

$$C_{notch}(s) = \prod_{i=1}^3 \frac{s^2 + 2\hat{\xi}_i \hat{\omega}_{n_i} s + \hat{\omega}_{n_i}^2}{s^2 + 2\hat{\omega}_{n_i} s + \hat{\omega}_{n_i}^2}, \quad (\text{A.1})$$

where $C_{notch}(s)$ is the transfer function of the notch filter, and $\hat{\xi}_i$ and $\hat{\omega}_{n_i}$ are, respectively, the damping ratios and natural frequencies of the resonance modes obtained by system identification in Section 3.4, 4.3, and 4.4. The design parameters values of the notch filter for each case are summarized in Table A.1.

Table A.1: Notch-filter design parameter values

	Simulations	Large-scale	Minaturized
$\hat{\omega}_{n_1}$	106	64	95
$\hat{\xi}_1$	5×10^{-3}	1×10^{-3}	2×10^{-2}
$\hat{\omega}_{n_2}$	170	102	230
$\hat{\xi}_2$	1×10^{-4}	1×10^{-4}	4.9×10^{-2}
$\hat{\omega}_{n_3}$	665	252	352
$\hat{\xi}_3$	1×10^{-3}	1×10^{-3}	4.7×10^{-1}

A.2 PID Controller Design

The standard PID controller is parametrized as:

$$C_{PID}(s) = K_p + \frac{K_i}{s} + \frac{K_d s}{\frac{1}{2\pi f_c} s + 1}, \quad (\text{A.2})$$

where $C_{PID}(s)$ is the transfer function of the PID controller and K_p , K_i , and K_d , are the proportional, integral, and derivative gains, respectively. f_c is the cut off frequency of the low pass filter used to deal with noise amplification limitations of the derivative term.

In PID controller, increasing proportional gain (K_p) reduces tracking error (O1). The integral term eliminates steady-state error (S1) and increasing integral gain (K_i) reduces tracking error (O1). The derivative term provides damping properties for closed-loop system and increasing derivative gain (K_d) increases stability margin (S2). The low-pass filter term limits high high-frequency controller gain caused by the derivative term. Decreasing f_c decreases high-frequency controller gain (S3).

The procedure used for designing PID controller is listed in the following:

1. set all parameters equal to zero.
2. increase K_p to improve (O1) until (S2) is violated. (P-controller)
3. increase K_i to improve (O1) until acceptable bandwidth is achieved.
4. set $f_c=10$ kHz as an acceptable cut off frequency.
5. set $K_d = \frac{(S3)-K_p}{2\pi f_c}$ to ensure satisfaction of (S3)
6. check (S2). If (S2) is satisfied, finish; else, decrease K_p slightly and go to 5.

De-tuning of PID controller was done by appropriately decreasing proportional and integral gains until the closed-loop system associated with OISs are stable. Due to conservativeness of the de-tuned PID controller, the derivative and low-pass filter terms are unnecessary. The parameters obtained by implementation of this procedure are shown in Table A.2.

A.3. Lead-lag Controller Design

Table A.2: Controller design parameters of the PID controller

	Simulations	Large-scale	Miniaturized
K_p	$7 \times 10^{-4} (6 \times 10^{-8})$	$1 \times 10^0 (1 \times 10^{-1})$	$1.2 \times 10^{-2} (3 \times 10^{-3})$
K_i	$5 \times 10^{-1} (1 \times 10^{-2})$	$4 \times 10^1 (4 \times 10^1)$	$1 \times 10^0 (5 \times 10^{-2})$
K_d	$1 \times 10^{-7} (-)$	$5 \times 10^{-3} (-)$	$2 \times 10^{-7} (-)$
f_c	$1 \times 10^4 (-)$	$3 \times 10^1 (-)$	$1 \times 10^4 (-)$

A.3 Lead-lag Controller Design

The standard lead-lag controller is parametrized as:

$$C_{ll}(s) = K_p K \frac{\frac{1}{z_{lead}} s + 1}{\frac{1}{p_{lead}} s + 1} + \frac{\frac{1}{z_{lag}} s + 1}{\frac{1}{p_{lag}} s + 1}, \quad (\text{A.3})$$

where $C_{ll}(s)$ is the transfer function of the lead-lag controller, K_p is the P-controller gain, K is the lead-lag controller gain, and K_d , z_{lead} and p_{lead} are, respectively zero and pole of the lead, and z_{lag} and p_{lag} are, respectively zero and pole of the lag.

The procedure used for designing PID controller is listed in the following:

1. set $K = \frac{10^2}{K_p K_t^*}$ for acceptable steady-state error and $\omega_b=0$.
2. increase ω_{bw} incrementally to improve (O1).
3. set $z_{lag} = \omega_{bw} \sqrt{K}$ and $p_{lag} = \omega_{bw} / \sqrt{K}$.
4. read ω_{gc} from open-loop bode plot and set $p_{lead} = \omega_{gc} \sqrt{\frac{(S3)}{K_p}}$ and $z_{lead} = \omega_{gc} \sqrt{\frac{K_p}{(S3)}}$ to ensure (S3).
5. check (S2). If (S2) is satisfied, go to Step 2; else, finish.

De-tuning of lead-lag controller was done by appropriately decreasing proportional gains K_p and K and bandwidth ω_{bw} such that the closed-loop system associated with OISs are stable. The parameters obtained by implementation of this procedure are shown in Table A.3.

A.4. LQG Controller Design

Table A.3: Controller design parameters of the lead-lag controller

	Simulations	Large-scale	Miniaturized
K_p	1.0×10^{-3} (1.0×10^{-4})	1.0×10^0 (1.0×10^{-1})	1.2×10^{-2} (1.0×10^{-2})
K	2.0×10^1 (1.0×10^1)	2.2×10^1 (2.2×10^1)	5.0×10^1 (2.0×10^2)
p_{lead}	2.8×10^3 (2.8×10^3)	5.3×10^2 (5.3×10^2)	9.3×10^2 (9.3×10^2)
z_{lead}	2.0×10^3 (2.0×10^3)	1.8×10^2 (1.8×10^2)	3.1×10^2 (3.1×10^2)
p_{lag}	2.2×10^{-2} (2.2×10^{-2})	1.7×10^0 (1.7×10^0)	2.1×10^0 (2.1×10^0)
z_{lag}	5.7×10^{-1} (5.7×10^{-1})	1.2×10^2 (1.2×10^2)	3.2×10^2 (3.2×10^2)

A.4 LQG Controller Design

The LQG servo controller minimizes the cost function

$$J = E \left\{ \lim_{\tau \rightarrow \infty} \frac{1}{\tau} \int_0^\tau (x^T Q_x x + u^T Q_u u + x_i^T Q_i x_i) dt \right\},$$

subject to system dynamics

$$\dot{x} = Ax + Bu + w$$

$$y = Cx + Du + v$$

where the process noise w and measurement noise v are Gaussian white noises with covariances Q_w and Q_v , respectively. In the cost function E designates expected value, x is the state vector, u is the control input vector, and x_i is the state variable associated with the integral of the tracking error.

The design parameters Q_x , Q_u , and Q_i are positive definite weighting matrices used to penalize states, control input, and tracking error, respectively. These weighting matrices are used to achieve performance objectives and meet performance specifications. Tracking error (O1) can be reduced by increasing Q_i . To increase stability margin (S2), Q_x should be increased. Finally, Q_u is increased to reduce control effort (O2) and avoid saturation due to noise amplification (S3).

De-tuning of LQG controller was done by decreasing Q_i until the closed-loop system associated with OISs are stable. The parameters obtained by implementation of this procedure are shown in Table A.4.

A.5. H_∞ Controller Design

Table A.4: Controller design parameters of the LQG controller

	Simulations	Large-scale	Miniaturized
Q_x	$1 \times 10^0 (1 \times 10^0)$	$1 \times 10^0 (1 \times 10^0)$	$1 \times 10^0 (1 \times 10^0)$
Q_u	$4 \times 10^1 (4 \times 10^1)$	$1 \times 10^2 (1 \times 10^2)$	$1 \times 10^0 (1 \times 10^1)$
Q_w	$1 \times 10^{-3} (1 \times 10^{-3})$	$1 \times 10^{-3} (1 \times 10^{-3})$	$1 \times 10^{-3} (1 \times 10^{-3})$
Q_v	$1 \times 10^{-3} (1 \times 10^{-3})$	$1 \times 10^{-3} (1 \times 10^{-3})$	$1 \times 10^{-3} (1 \times 10^{-3})$
Q_i	$1 \times 10^5 (4 \times 10^{-2})$	$5 \times 10^5 (1 \times 10^4)$	$1 \times 10^5 (1 \times 10^1)$

A.5 H_∞ Controller Design

The H_∞ controller minimizes the H_∞ norm of the system from r to $z = [e_w^T \ u_w^T]^T$ in A.1.

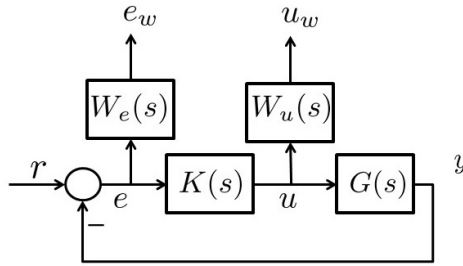


Figure A.1: Weighted control system configuration H_∞ controller design

The design parameters $W_e(s)$ and $W_u(s)$ are weighting functions used to penalize tracking error and control input, respectively. These weighting functions are used to achieve performance objectives and meet performance specifications. W_e is used to improve (O1) and meet (S1) and (S2). W_u is used to achieve (O2) and meet (S3). To avoid high order controller (O3), we propose using constant W_u and first order W_e parameterized as follows [70]:

$$W_e(s) = \frac{s/M_H + \omega_b}{s + \omega_b M_L}, \quad (\text{A.4})$$

where M_L , M_H , and ω_b are design parameters which, respectively, denote low-frequency gain, high-frequency gain, and bandwidth of W^{-1} . To reduce steady state error (S1), M_L should be reduced. Tracking error (O1) can be reduced by increasing ω_b which corresponds to bandwidth. To increase stability margin (S2), peak of sensitivity M_H should be reduced. Finally, W_u is taken as a constant gain, and it is increased to reduce control effort

A.6. Robust Controller Design

(O2) and avoid saturation due to noise amplification (S3).

De-tuning of H_∞ controller was done by decreasing ω_b until the closed-loop system associated with OISs are stable. The parameters obtained by implementation of this procedure are shown in Table A.5. In the following, ω_b is reported in Hz and the rest of the parameters are in dB .

Table A.5: Controller design parameters of the H_∞ controller

	Simulations	Large-scale	Miniaturized
M_L	-4×10^1 (-4×10^1)	-4×10^1 (-4×10^1)	-4×10^1 (-4×10^1)
ω_b	1×10^2 (2×10^0)	7×10^1 (2×10^{-1})	1×10^2 (1×10^0)
M_H	2×10^0 (2×10^0)	2×10^0 (2×10^0)	2×10^0 (2×10^0)
W_u	-4×10^1 (-4×10^1)	1×10^0 (1×10^0)	-3×10^1 (-3×10^1)

A.6 Robust Controller Design

The robust controller design theories, namely μ -synthesis and robust H_∞ rely on a similar design parameters and methodologies as the H_∞ controller design method, except for the fact that there is no de-tuning procedure involved because the theories themselves guarantee robust closed-loop stability and performance against uncertainties. Table A.6 and Table A.7 shows the controller design parameters obtained for μ -synthesis and robust H_∞ controllers, respectively.

Table A.6: Controller design parameters of the μ -synthesis controller

	Simulations	Large-scale	Miniaturized
M_L	-4×10^1	-2×10^1	-4×10^1
ω_b	8×10^1	2×10^1	8×10^1
M_H	2×10^0	2×10^0	2×10^0
W_u	2×10^2	3×10^1	-1×10^1

As the primary objective of the OIS is tracking (O1). Therefore, the general approach to design of all controllers have been to minimize the tracking error until atleast one of the performance specifications (S2) and (S3) are violated. In this regard, Table A.8 summarizes the general trade-off (positive (+) or negative (-) effect) that each of the introduced controller design parameters have on the control objectives and specificatins.

Table A.7: Controller design parameters of the robust H_∞ controller

	Simulations	Large-scale	Miniaturized
M_L	-4×10^1	-2×10^1	-2×10^1
ω_b	8×10^1	5×10^0	1×10^0
M_H	2×10^0	2×10^0	8×10^0
W_u	2×10^2	3×10^1	1×10^1

Table A.8: Summary of performance trade-offs associated with controller design parameters

	O1	S2	S3
K_p	+	-	-
K_i	+	-	-
ω_{bw}	+	-	N
Q_i	+	-	-
Q_u	-	+	+
Q_w	+	+	-
Q_v	-	N	+
M_L	-	+	+
ω_b	+	+	-
M_H	+	-	-
W_u	+	-	-

Appendix B

Hand-shake Disturbance Database

This section explains details of hand-shake disturbance database. This database is used in the time-domain setup (Section 4.1.2) as well as control objective definition (Section 2.3). The explanation includes properties of hand-shake signals in time-domain and frequency-domain.

B.1 Time-domain Signals

Hand-shake disturbance data are collected from built-in gyro-enhanced motion sensors of a mobile phone while holding the mobile phone to take a photograph. A database is prepared by hand-shake disturbance data of 5 different people. Time-domain signals of are displayed in Figure B.1, where HSD stands for hand-shake data.

B.2. Frequency-domain Spectra

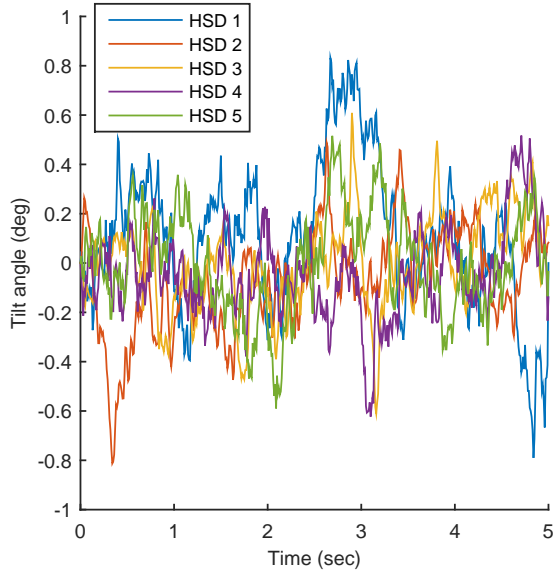


Figure B.1: Time-domain signals of hand-shake disturbance database

The DC component was removed since the goal of image stabilization is to compensate for involuntary hand-shake and not intentional pan. The signals are of relatively random nature with a magnitude of typically less than 1 degree.

B.2 Frequency-domain Spectra

To validate the database in the frequency-domain, a spectral analysis is performed on this database through discrete Fourier transform [7]. Figure B.2 shows the spectral density for each of 5 hand-shake data in the data set. As shown, the spectral density of different hand-shake data are consistent with each other. In general, the dominant frequencies are below 20 Hz which is compatible with results published in the literature [18, 58]. The sampling frequency of the gyro-enhanced motion sensor was 100 Hz, and thus according to the Nyquist-Shannon sampling theorem [7], only frequencies below 50 Hz were considered.

B.2. Frequency-domain Spectra

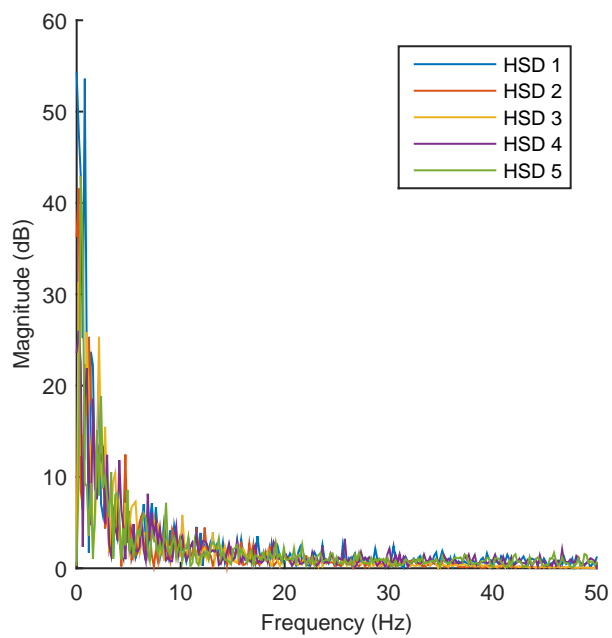


Figure B.2: Frequency-domain spectra of hand-shake disturbance database

Appendix C

Model Parameter Values

C.1 Uncertainty Model Parameter Values

The numeric values of the parameters used for the dynamic uncertainty model of OIS ($G(s, \delta)$ in 3.1) are tabulated in Table C.1. In this table, the values used for simulations, large-scale, prototype, and small-scale prototype are presented in separate columns.

Table C.1: Model parameter values

	Simulations	Large-scale	Minaturized
$\omega_{n_1}^*$	106	64	95
$\xi_1^*/[\xi_1 \ \xi_1]$	5×10^{-3}	1×10^{-3}	$[2 \ 3] \times 10^{-2}$
$\omega_{n_2}^*$	170	102	230
$\xi_2^*/[\xi_2 \ \xi_2]$	1×10^{-4}	1×10^{-4}	$[3 \ 5] \times 10^{-2}$
$\omega_{n_3}^*$	645	230	343
$\xi_3^*/[\xi_3 \ \xi_3]$	1×10^{-3}	1×10^{-3}	$[1 \ 3] \times 10^{-2}$
$\omega_{n_4}^*$	665	252	352
$\xi_4^*/[\xi_4 \ \xi_4]$	5×10^{-3}	1×10^{-3}	$[1 \ 5] \times 10^{-2}$
k_{shift}^*	0	0	0
k_{tilt}^*	4×10^5	4×10^0	4×10^2
k_{shift}	8×10^4	2×10^{-1}	2×10^1
k_{shift}	-8×10^4	-2×10^{-1}	-2×10^1
$\overline{\omega_{n_2}}$	180	97	221
ω_{n_2}	160	107	341
c_k	1.7	1.7	1.2
c_1	1.1	1.1	0.3
c_3	0.3	0.3	0.2
c_4	0.4	0.4	0.8
τ	1.1	1.1	1.1

C.2. Actuator Model Parameter Values

C.2 Actuator Model Parameter Values

The numeric values of the parameters used for mechanical design and dynamic uncertainty modeling of OIS are tabulated in Table C.2. In tables, the values used for simulations, large-scale, prototype, and small-scale prototype are presented in separate columns.

Table C.2: Moving-magnet actuator parameter values

	Simulations	Large-scale	Minaturized
Inner diameter (mm)	1.0	2.06	0.5
Outer diameter (mm)	4.1	14.4	3.3
Height (mm)	4.0	21.5	4.0
Wire gauge (AWG)	36	28	36
Wire turns (-)	372	960	347
Diameter (mm)	2.5	6.34	1.6
Thickness (mm)	0.65	1.6	0.8
Air-gap at eq. (mm)	0.25	1	1

The moving-magnet actuators from current inputs to torque output display static nonlinear behavior. Therefore, we will model the moving-magnet actuator as a static nonlinear map, i.e., the 'Look-up Table' block in Figure 2.2, and obtain its inverse map to compensate its nonlinearity.

The model of the moving-magnet actuators is developed considering the currents of coils as the input and the torque generated on the lens-platform about the x -axis as the output. Figure C.1 illustrates the tilt actuation about one axis. A torque T is generated on the lens-platform by forces F generated on the magnets by coils with the configuration shown.

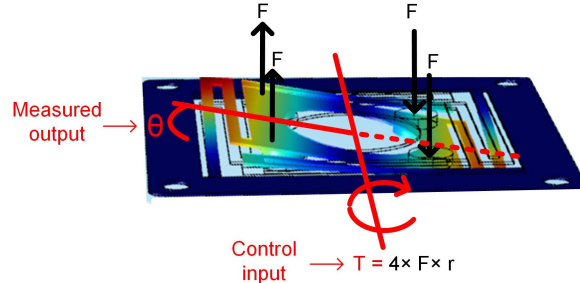


Figure C.1: Tilt actuation

C.2. Actuator Model Parameter Values

The forces F necessary to generate a torque of T can be obtained as:

$$F = T/4r. \quad (\text{C.1})$$

The force generated on the magnet is a function of the current of the coil and the air-gap. According to Lorentz law, force is linearly proportional to the current, and due to Amperes law, it is inversely related to the air-gap. To quantitatively obtain this relationship, finite-element method magnetics (FEMM) software [40] is used for the parameters of moving-magnet actuators in Table C.2.

Figure C.2 shows the inverse relationship of the force with the air-gap for a constant current of 1 A as obtained by FEMM for the large-scale prototype as an example.

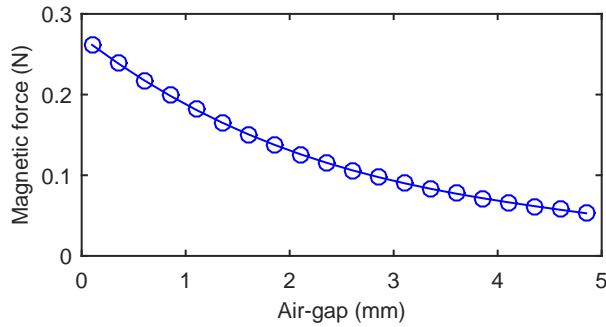


Figure C.2: Force–air-gap relationship ($i = 1$ A)

This relationship is used as a look-up table denoted by $p(z)$ where z is the air-gap. Hence, the force generated on each magnet can be described as $F = p(z)i$. When the lens-platform is tilt about x -axis for , air-gaps of pairs of coil/magnet on two sides of this axis can be calculated as $z_{1,3} = z_0 - rsin(\theta)$ and $z_{2,4} = z_0 + rsin(\theta)$, where z_0 is the equilibrium air-gap, r is the distance of magnets from central axes, and the z_k ($k = 1, 2, 3, 4$) is the air-gap of the k -th moving-magnet actuator. These air-gap values of each actuator is used to calculate the required current to be applied to its coil (i_k) by $i_k = F/p(z_k)$.